UNIVERSITÀ DEGLI STUDI DI PADOVA

DIPARTIMENTO DI FISICA E ASTRONOMIA "GALILEO GALILEI"

CORSO DI LAUREA MAGISTRALE IN ASTRONOMIA

Analysis of skylights and lava tubes on Mars

RELATRICE:

Prof.ssa Monica Lazzarin

CORRELATORI:

Dr. Gabriele Cremonese

Prof. Junichi Haruyama

Dr. Riccardo Pozzobon

Dr.ssa Cristina Re

LAUREANDA:

Chiara Tettamanti

Anno Accademico 2018/2019

Abstract

Remote sensing data show the presence of candidate lava tubes on Mars and Moon, suggested by the presence of skylights and sinuous alignments of depressions. Due to the similar characteristics of basaltic volcanism on Terrestrial bodies, it is expected that lava tubes have similar morphologies and origin among them. Only recently, because of the increasing amount of geophysical data and high resolution images, it was possible to perform comparisons between lava tubes on different planetary bodies with implications on the study of planetary volcanology, habitability and astrobiology. Indeed, high resolution orbital images and stereo Digital Terrain Models (DTMs) of the last decade offer the possibility of studying the morphology of these structures, which develop almost parallel to the topography at depth, detecting them from their collapsed sections.

In this work was considered an area on Mars, at North of Arsia Mons, where it was mapped and analysed small skylight-like depressions (< 100 m) resembling those related to overcrusted lava tubes on Earth. Orbital images used to detect lava tubes and perform measurements are NASA's Mars Reconnaissance Orbiter Context Camera (CTX) and High Resolution Imaging Science Experiment (HiRISE). The depths of collapsed sections were estimated exploiting the length of the shadow cast of the rim. From high resolution DTMs realised specifically for selected locations from HiRISE and CaSSIS stereo pair images, it was estimated the reliability of measurements of the depth, which do not agree statistically but for the analysis performed are useful as well.

It was possible to verify the width of the tunnel when in presence of elongated depressions: their minor axis represents its maximum width and the major axis the direction of the conduit. The calculated asymmetry ratio (depth/width) conveys information on the ellipticity of the conduit and, in turn, of its formation mechanism. The candidate lava tubes were interpreted to have an overcrusted origin because of the presence of small levees along their path and the relative shallow depth of sinuously aligned skylights/depressions.

For the first time it was realised a comparison between Martian overcrusted lava tubes and the Terrestrial analogue Kazumura cave (Hawaii). As expected from implications of lower gravity on Mars, Martian lava tubes are larger in width and length, thus involving bigger volumes of lava. The asymmetry ratio is different: from morphological measurements of the interior of Kazumura cave, resulted an almost circular section, while the Martian lava tubes show elliptical sections, but this can be interpreted as an effect given by the presence of debris at the bottom of the conduit, which indicate that collapses occurred after lava emplacement, or a not completely drained tunnel.

The dimensions of the conduits were used to estimate the value of the yield strength of lava, which is assumed to behave as a Bingham fluid. Three models of lava tubes were realised to explain different types of formation and actual conditions. Using the measured depth and assuming a drained lava tube, the value of yield strength is $\tau_1 = 1425.78 \pm 7.45$ Pa; considering a circular section conduit filled of lava during emplacement and then drained, it was obtained $\tau_2 = 742.62 \pm 2.78$ Pa; regarding the model of free lava flow with circular section tunnel not drained and filled with debris the value is $\tau_3 = 1749.52 \pm 15.86$ Pa.

From the detailed measurements of voids in the subsurface and the dimensions of lava tubes, it is possible to get insights on volcanism on Mars, with implications on future space missions.

Contents

1 Introduction **4**

2 Geological context **5**
2.1 Volcanism on Mars 5
2.2 Tharsis region 6
2.3 Lava tubes 9

3 Motivation **13**

4 Data and methods **14**
4.1 Instrumentation description 14
4.1.1 MRO HiRISE 14
4.1.2 MRO CTX 15
4.1.3 TGO CaSSIS 15
4.1.4 MOLA 16
4.2 Identification and location of lava tubes and skylights 17
4.3 Measurement of Terrestrial skylights 23
4.4 Estimate of the yield strength 23
4.5 Digital Terrain Models from stereo pair images 27

5 Results **29**
5.1 Comparison between Martian and Terrestrial skylights 32
5.2 Yield strength 34

6 Future works and applications **39**

7 Conclusions **41**

8 Tables **42**

References **53**

1 Introduction

The first scientist describing a lava tunnel, having inspected it, was probably Eggert Olafsen (1774-1775) (Kempe, 2012) in Iceland, and later it was observed a forming lava tube in Hawaii. Lava tubes are described as tunnels that develop in the subsurface, almost parallel to the ground. It is difficult to detect them because they usually do not show features on the surface, unless they collapse forming skylight-like apertures on the ground.
Since Oberbeck et al. (1969) interpreted collapsed lunar rilles as lava tubes, the interest on these volcanic structures has grown up because of their potential in many scientific fields. Indeed, their presumable pristine condition, with an environment containing preserved lava composition, textures and even volatiles are important case studies for the evolution of the planetary body. Furthermore, their insulation properties can be exploited for space exploration.

Since basaltic volcanism on rocky planets is similar, it is expected the existence of lava tubes also on other planets, with analogies in their formation and morphologies. The characteristics and utilities of lava tubes are mainly discussed for the Moon and Mars, due to their geological and environmental relative closeness to the Earth.
Technical limitations of orbiting instruments, such as the spatial resolution and areal coverage, have hindered the detection of lava tubes and their collapses, but in the last decades there was a great advance in technology, thanks to NASA's and ESA's space missions, as Mars Reconnaissance Orbiter and ExoMars.
Bleacher et al. (2007a, 2007b) identified numerous tube-fed lava-flow systems on the flanks of Olympus Mons and elsewhere in the Tharsis region of Mars and inferred some collapsed lava-tube sections to be skylights, Cushing (2012), with the aim of finding caves on Mars, has identified many pit craters, some of which are lava tubes entrances. Every identified pit crater is listed in the Mars Global Cave Candidate Catalog (MGC^3) (Cushing, 2017), which appears in a conference proceeding but it is not published, yet. On the Moon Haruyama et al. (2009) was the first to discover a small skylights, the Marius Hill Hole, that has been interpreted as an intact lava tube.
This work focuses on the morphology of skylights and lava tubes on Mars, in the region at North of Arsia Mons, and their comparison with a terrestrial analogue, Kazumura cave in Hawaii. Afterwards, it was estimated the rheological parameter of yield strength, using three different models of lava tubes.
A brief geological introduction to martian volcanism, the description of the considered area and the formation and characteristics of lava tubes are in section 2, in section 4.1 there is the description of the instruments that acquired the images on which the analyses were performed and in section 4.2, 4.3, 4.4 are explained how they were executed. In section 5 are summarised the results and it is also presented an alternative method for the performed measurements of the lava tubes and skylights morphologies, exploiting the opportunity of generating, for specific locations, Digital Terrain Models (DTM), described in section 4.5.

2 Geological context

2.1 Volcanism on Mars

Volcanism on Mars lasted for a very long time, from the Late Noachian to the late Hesperian and in some regions, such as Tharsis and Elysium, until the most recent Amazonian (Head et al., 2001) (figure 1). The division in periods of Martian history

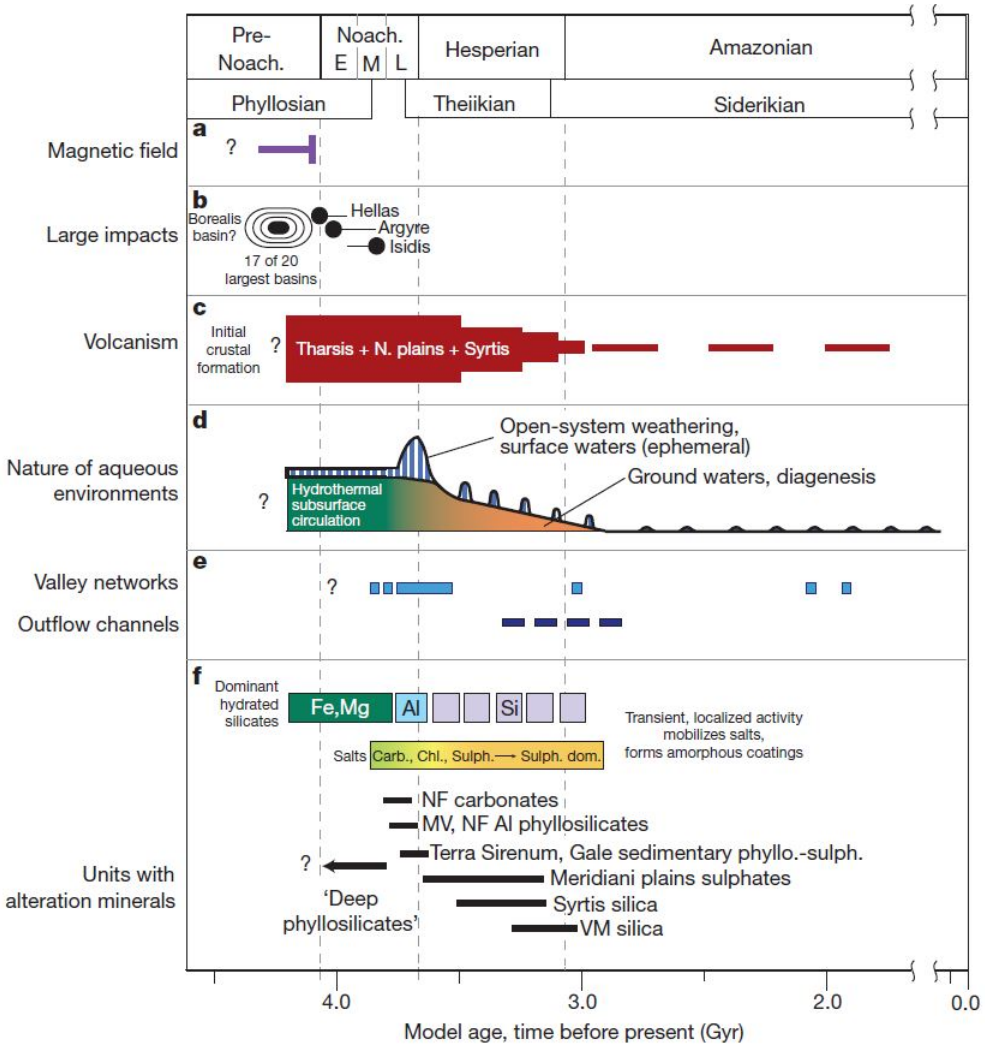

Figure 1: Chronological contextualisation of volcanic processes on Mars. Presence of a magnetic field (a), impact cratering (b), volcanism (c), changing nature of environments hosting liquid water (d), evidence of liquid water (e) (f). NF, Nili Fossae; MV, Mawrth Vallis; VM, Valles Marineris; Carb., carbonates; Chl., chlorites; Sulph., sulphates. (Ehlmann et al., 2011)

was performed considering the impact crater size frequency distribution, which is based on the fact that the production function for impact craters, that considers the number of craters/km^2 on a surface in a given time as a function of diameter, is known in the inner Solar System and it is based on the Lunar chronology obtained for the Moon using the impact craters and samples collected on the surface (Neukum et al., 2001). Ivanov (2001) derived the cratering rate of Mars relative to the Moon,

but due to the lack of samples from Mars whose context and provenance are known, an estimate of the absolute ages can not be reliable. Considering different models, the transition from Noachian to Hesperian is placed 3.5 Gyr ago and the passage from Hesperian to Amazonian 2.9-3.3 Gyr ago. Regardless the model used, the peak in endogenic activity was before 3 Gyr ago (Hartmann and Neukum, 2001).
Despite volcanism on the Earth, it seems that currently on Mars there is no more volcanic activity, and the reason can be found in its minor amount of primordial energy, which is proportional to the mass of the body, and to a more rapid dissipation of energy, that is related to the ratio between area and volume of the planet.
Volcanism is important for Mars history because during its long activity has not only reshaped the landscape but has also affected the evolution and chemistry of the atmosphere and altered the rocks and soils at the surface. The atmosphere is largely a product of the outgassing of the interior. Formation of the massive volcanic pile, which is Tharsis, must have been accompanied by large-scale release of volatiles, such as water, from the interior (Carr, 2007).
From studies on terrains of different ages, by the exposure of layers from craters or faults, it seems that the crust of Mars was firstly formed by poorly consolidated material, which can be related to explosive volcanism, and later on, during the Hesperian era, volcanism transitioned to more effusive styles of eruptions, which is manifested by superficial lava flows composed of effusive lava (Bandfield et al., 2013).
Martian lava is almost certainly basaltic in composition, as Terrestrial and Lunar ones, so it produces basalt, which is a dark fine-grained igneous rock with low content in mass of silica (45-55%) and rich in magnesium and iron (mafic). The mantles of the terrestrial planets are all thought to have a similar composition, one that resembles that of chondritic meteorites from which the planets are believed to have formed. Partial melting of material of chondritic composition yields basaltic magma, but the composition of igneous rocks can vary depending on the processes at which magma undergoes during the rising, for example the partial crystallization (Carr, 2007).
There are many proofs in favour of the basaltic composition of igneous rocks. Investigations performed with the Thermal Emission Spectrometer (TES) on board of the Mars Global Surveyor (MGS), distinguished two types of terrain: one was interpreted as basalt and the other as andesite (Bandfield et al., 2000), which has an higher content of silica and forms in subductive zones on Earth of which there is no evidence on Mars. Further investigations revealed that the improbable andesite was weathered basalt (Wyatt and McSween, 2002). Moreover, samples in Gusev site examined by the Spirit rover have a basaltic composition (McSween et al., 2004), as also Martian meteorites whose origin was reliably identified on the basis of similarity between gas compositions in their vesicles with composition of Martian atmosphere measured by instruments on satellites.

2.2 Tharsis region

It is possible to recognise some important volcanic regions on Mars, such as Tharsis and Elysium, which contain the biggest volcanoes in the Solar System. Consider-

ing the absence of evidence of plate tectonics, these important structures can have formed from a tectonism driven by plumes that, differently from the Terrestrial example of Hawaiian islands, allowed the stacking of volcanic material (Carr, 2007). The Martian thicker lithosphere, lower gravity and lower atmospheric pressure than Terrestrial ones, enable the construction of such high structures, that can reach, in the case of Olympus Mons, 22 km in height (Plescia, 2004). However, volcanic deposits on Tharsis, that dominate the western hemisphere of Mars, create a detectable gravity anomaly (Neumann et al., 2004) and fractures of the stressed lithosphere, which cannot bear the volcanic load and led to the failure of the isostatic compensation. These extensional fractures radiate outwards the Tharsis region and are also visible around the volcanoes with concentric layout (Tanaka et al., 2014).

The Tharsis region is the locus of Tharsis Montes, the largest volcanic edifices and amongst those that present a long-lasting volcanic activity up to recent geologic time. They are, from southwest to northeast, Arsia, Pavonis and Ascraeus Montes (figure 2). The main shields formation ended about 3.55 Gyr ago and followed many episodes of surface modification, which covered the edifices with many layers of lava flows (Werner, 2009).

These edifices have enormous widths (350 to 400 km) and small inclinations ($< 10°$) which make them resemble to Terrestrial shield volcanoes, examples of which can be found in Hawaii. The similarity is also found in others subsidiary features, such as calderas, lava channels, flow fronts, and collapse pits, as well as the large extension of lava flows that form plains, which can be related to effusive style eruption, characterised by low viscosity lava.
The region described in this thesis is located at north of Arsia Mons and the features studied are, reasonably, products of an eruption of this volcano.
Arsia Mons is 400 km across, has a summit elevation of 17.7 km (Plescia, 2004). For comparison, the largest volcano on Earth, Mauna Loa in Hawaii, is roughly 120 km across and stands 9 km above the ocean floor.
Crater dating suggests that the caldera floor is 128 Myr old (Werner, 2009). The flanks have an inclination of roughly 5°. On the northeast and southwest flanks, numerous pits have coalesced to form rifts from which large volumes of lava have erupted forming broad aprons over the adjacent plains, indicating that apron flows are younger than those on the shield. There are numerous grabens almost radial to Arsia Mons and has been interpreted as surface manifestations of large dikes radial to the central magma reservoir of Arsia Mons (Wilson and Head III, 2002).
Martian magma chambers are supposed to be located deeper than on Earth and also to be larger, as consequences of the lower gravity on Mars. The different value of gravity, thus, affects the volumes involved in volcanic activity that must be larger (Pozzobon et al. (2015) and references therein). As a result there is the expectation of higher effusion rates and thicker lava flows to allow the streaming for given magma properties. Such thick lava flows can reach, always due to low gravity, larger distances than on Earth (Wilson and Head III, 1994).

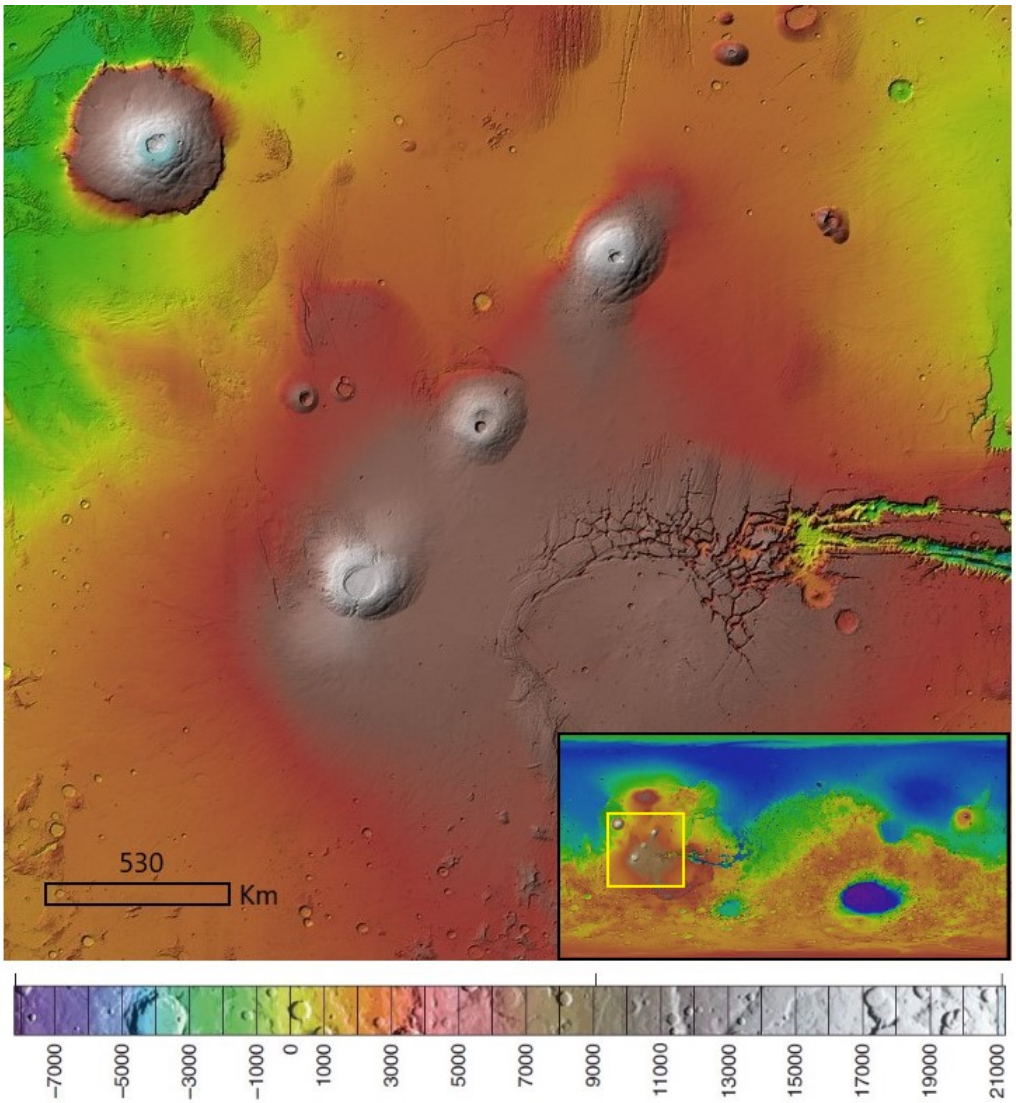

Figure 2: Tharsis Montes and Olympus Mons with information on elevation from MOLA data.

Figure 3: Section of Kazumura cave. *Photo by Dave Bunnel*
`www.vulcanospeleology.org/pgkazu`

2.3 Lava tubes

Lava, during its emplacement, can give origin to lava tubes, also called lava tunnels or pyroducts, which are conduits in the near subsurface that run approximately parallel to the surface (Kempe et al., 2010). They are usually linked to high viscosity lava of pahoehoe type. The roof of these structures can collapse during the activity or after the end of it, leaving possible entrances to caves when fallen material does not seal them (Cushing et al., 2015).
Cross sections of these tunnels (figure 3) are usually arched, rounded, elliptical, or keyhole shaped due to accretion of lava to the sidewalls and the downcutting of lava flows into the underlying rocks. In fact, while lava flows, it erodes the surrounding rock generating an underground canyon.

With the explorations of lava tubes on Earth, it was possible to discover a wide variety of patterns: single-trunked, double or multiple-trunked, superimposed-trunked systems (Kempe, 2012).
Single trunk systems are the most common type of lava tube and they are fed by one eruption. The size of the tunnel depends on the effusion rate and on the length of the activity which is related to the effects of thermal erosion.
Double-trunked systems are composed of two lava tunnels, active side by side at the same time and fed by two separate eruption points. Such tunnels can interact.
Superimposed-trunked category includes lava tunnels that are superimposed on different levels and cross each other, being active at the same time. Usually the tube at the top drains faster and lava continues to flow in the tubes below. Such systems could arise when a volcanic vent increases its output volume during an ongoing eruption and a new level of independently operating tunnels is built.
The formation of lava tubes is not clearly understood neither on Earth, but two types of origin are hypothesise: inflationary and overcrusted lava tubes (Kempe et al., 2010).
Inflationary lava tubes form when the thin sheets of lava, that previously covered

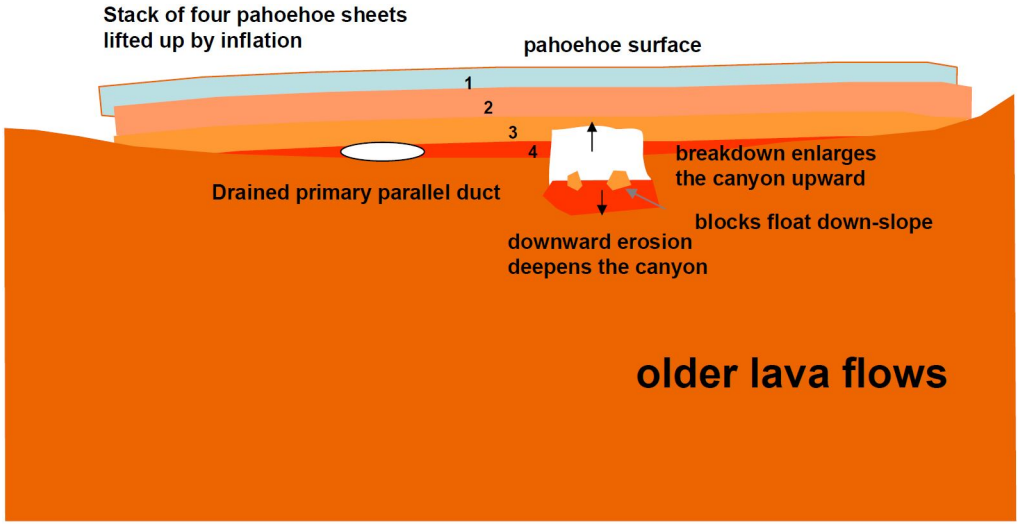

Figure 4: Representation of the section of an inflated lava tube. (Kempe et al., 2010)

the surface and solidified, are lifting up ("inflated") by a subsequent flow. Next, the flow expands in the direction of least resistance and erodes downward the tube, deepened it. A consequence is that there is almost always a gas-space above the lava river (figure 4).

Lava tubes can also develop from the crusted over of lava channel by blocks and slabs already in the solidified form that float and then stuck on the surface of the river. This layer is highly porous and not stable, but it is strengthened by injection of molten lava from below. Moreover, the porosity allow the air to circulate under the roof and to cool down, until solidification, a small layer of some centimetres of flowing lava that stabilise the roof. Later flows on the surface can reinforce further the stacked material that however remains stable only from buoyancy. So, if the tube remains drained or partially drained the stable part of the roof is only composed of the later flows that covered the primary roof (figure 5). Overcrusted lava tube can form also from closure of a lava channel by lateral shelf accretion. But this method requires a calm river, so probably it is enrolled in the construction of a secondary roof rather than a primary one. This type of lava tube is usually nearer to the surface and has a smaller and rounder section than inflationary lava tubes.

On Mars, lava tubes are observed near the vents of the most important volcanoes, and their expected difference from Terrestrial ones are once again dominated by the lower gravity. In fact, they should have larger dimensions due to higher effusion rates and are presumed to be more stable. Blair et al. (2017) obtained that cavities under Lunar gravity can remain stable until the kilometre size. Given that the Martian gravity is between the Lunar and Terrestrial one, on Mars are expected lava tubes of intermediate dimension between those on the Moon and Earth. In figure 6 it is shown a comparison between lava tube collapses on Earth and on Mars.

The analysis of these features on Mars can be currently realised with orbital images, that in the last decades had huge improvements, trying to spot collapses of them (figure 7). Indeed, in most of the cases, their presence can be guessed only with collapses, that, together with possible inflation of the terrain, is usually the only feature on the surface that reveal the presence of lava tubes.

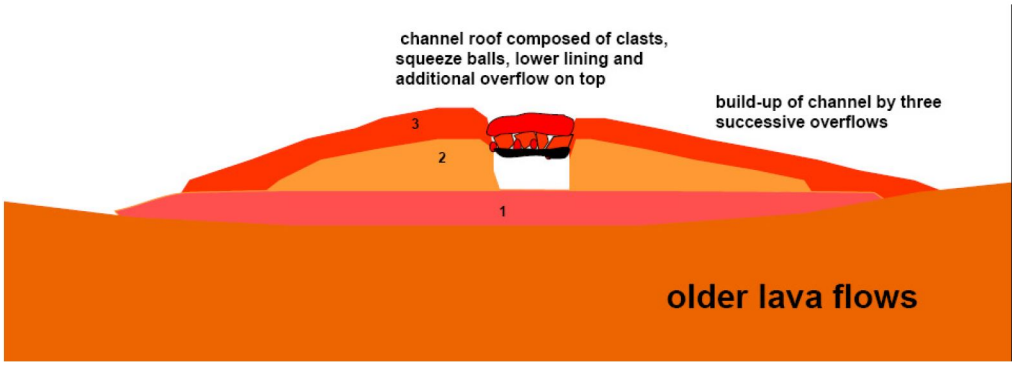

Figure 5: Representation of the section of an overcrusted lava tube (Kempe et al., 2010)

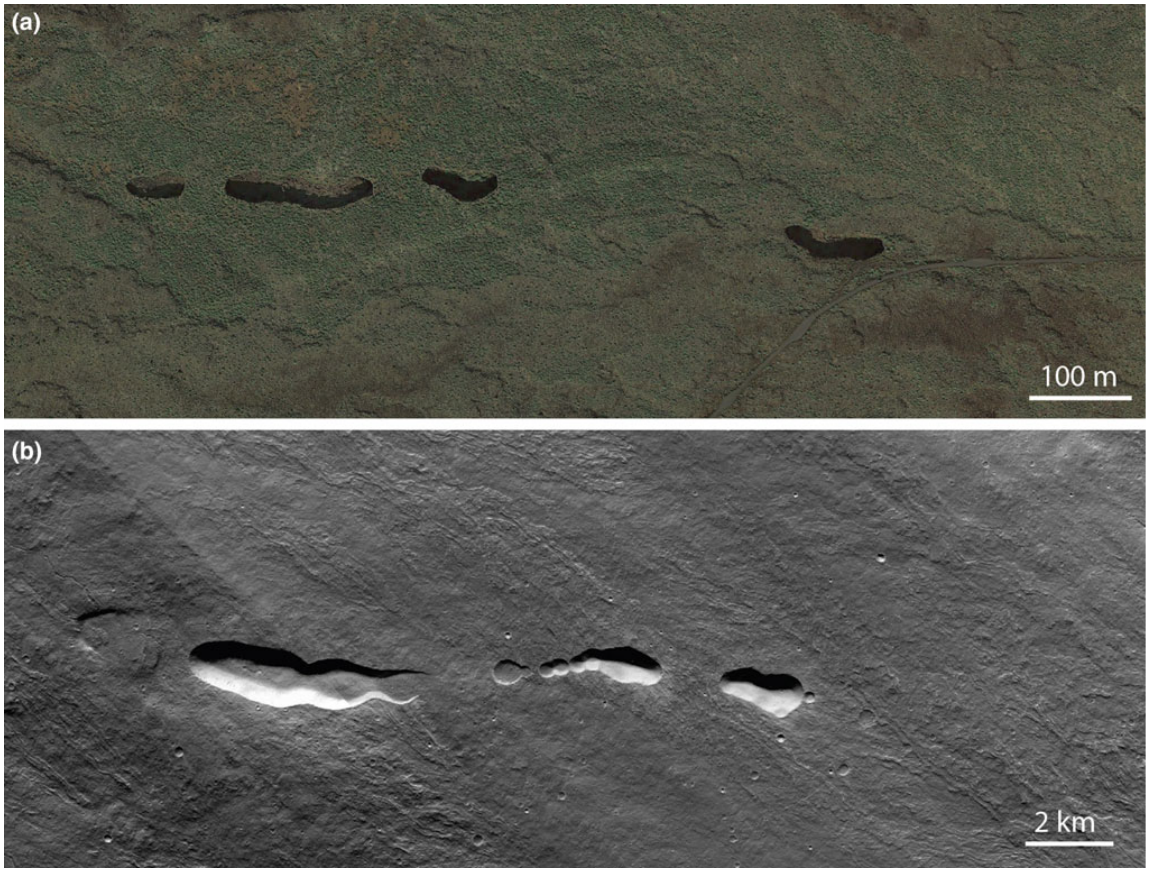

Figure 6: Collapses of Corona lava tube system in Lanzarote (Spain) (a), compared to analogue collapses on the flanks of Olympus Mons on Mars (b). Note the difference in scale. (Sauro et al., 2019)

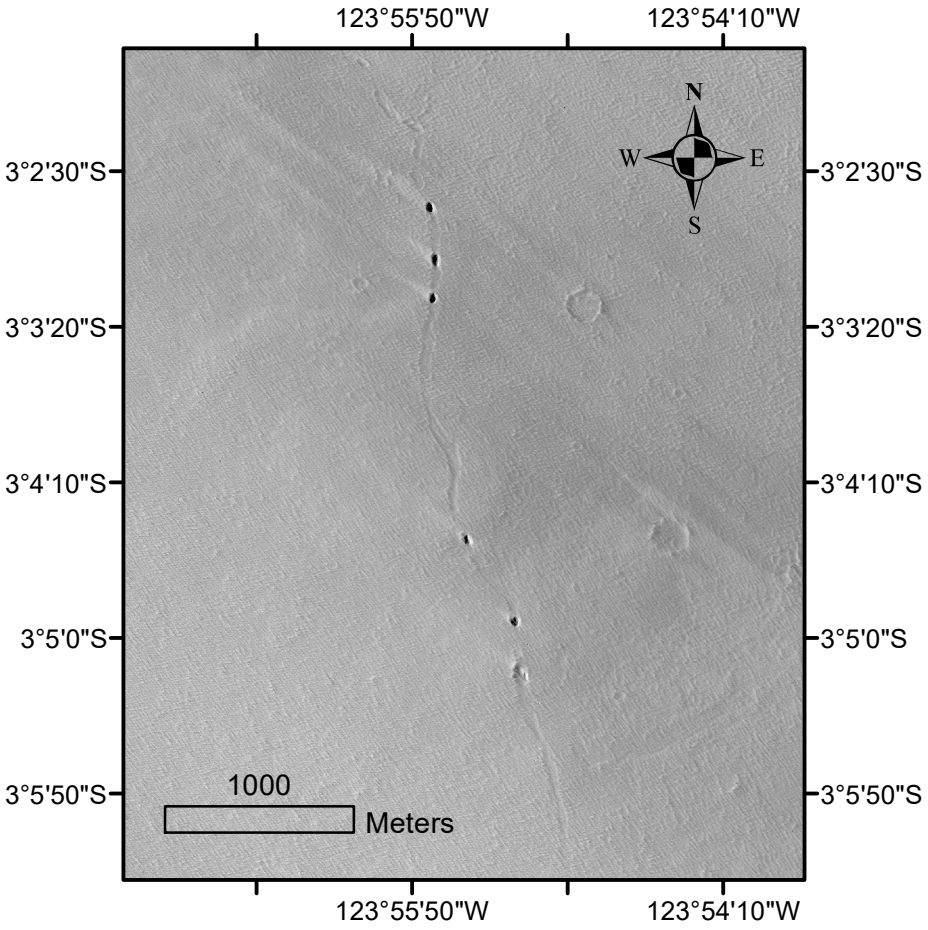

Figure 7: Example of overcrusted lava tube on Mars collapsed in 5 points. HiRISE image: ESP_037232_1770.

3 Motivation

The widespread network of lava tubes at north of Arsia Mons considered in this thesis gives the opportunity of measuring the morphology of these volcanic structures. Morphological properties of the detected skylights, whose coordinates are already listed in the Mars Global Cave Candidate Catalog (MGC^3) (Cushing, 2017), are needed to infer generic characters of underlying lava tubes, that may extend intact for several kilometres considering the high stability of the structures discussed in section 2.3.

Indeed, since lava tubes are a product of volcanic activity, from their properties it is possible to get insights on volcanism on Mars, which influenced the evolution of Mars for a long time. The length, width and height of lava tubes and their comparison with Terrestrial analogues can give an idea of the volumes involved in the eruptions and the mechanisms associated to their formation.

Widen the catalog of skylights together with their morphological properties measured on new available high resolution images, is useful to provide a criteria for distinguishing the different origin that a skylight-like depression can have: volcanic (from overcrusted or inflated lava tubes), volcano-tectonic or purely tectonic (Cushing, 2012). Moreover, from the detection of skylights it is possible to discover caves on Mars that could be interesting targets for future missions, since until now they were studied only from orbital images without the possibility of exploring their interior where keys to the geological, paleohydrological, and possibly biological history of Mars could be found.

The dimensions of the lava tubes, as well as the study of the terrain on which they develop, give the opportunity of estimating the rheological parameter of yield strength with a different method than the usual one, which consists in measuring the dimensions of solidified flows on the surface. Thus, it is provided a term of comparison to deduce the chemical composition of lava, which is related to the tectonic mechanism responsible for the volcanism on Mars. From the style of lava flow, which depends on lava composition, eruption temperature and effusion rate, can be deduced the class of the volcano (Griffiths, 2000).

4 Data and methods

Present-day high resolution images of Mars surface are available from numerous instruments on board different space missions and this thesis takes advantage of these data with the purpose of studying features of dimensions less than 100 m.
Images with the highest resolution (∼0.25 m/pixel) were taken by Mars Reconnaissance Orbiter's (MRO) High Resolution Imaging Science Experiment (HiRISE), which, however, poorly covers Martian surface (on 01/01/18 it was covered 2.92% of the surface (McEwen, 2018)). For this reason images with lower resolution taken by Mars Reconnaissance Orbiter's Context Camera (CTX) and Trace Gas Orbiter's Colour and Stereo Surface Imaging System (CaSSIS) were also helpful in order to carry out effectively the analysis of skylights and collapsed lava tubes sections on the surface of Mars.

4.1 Instrumentation description

4.1.1 MRO HiRISE

High Resolution Imaging Science Experiment (HiRISE) is on board the MRO which was launched on 12th August 2005 and entered Mars orbit on 10th March 2006. At the altitude of 300 km, the resolution of HiRISE images is 30 cm/pixel (McEwen et al., 2007).
HiRISE is a push-broom imaging sensor with 14 staggered CCDs (ten red, two blue green (BG), and two near infrared (NIR)) each composed of 2048 × 128 pixels and overlapped by 48 pixels to provide full swath coverage without gaps. Referring to figure 8 for the layout of CCDs on the focal plane, the effective swath width is of 20.048 pixels for the RED images and 4.048 pixels for the BG and NIR images. The BG and NIR channels overlap with the central two RED CCDs to provide 3-colour coverage.

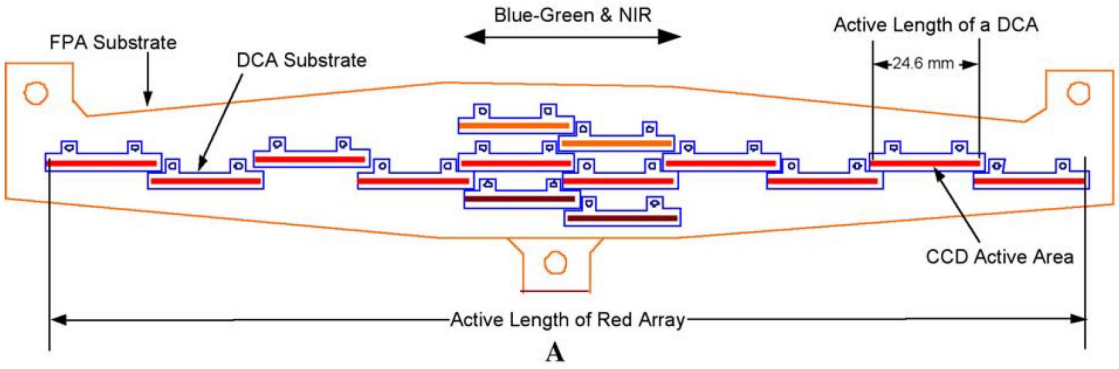

Figure 8: Locations of the 14 CCDs on the focal plane. (McEwen et al., 2007)

The telescope has an aperture of 50 cm and three astigmatic mirrors. Observations may be acquired in an interactive mode (IO): an example is related to the necessity of tilting the spacecraft up to 30° off nadir to obtain an optimal stereo geometry. This can be reached if one of each pair of images is acquired at an inclination greater than 10° off nadir in order to achieve a good base-to-height ratio

and also stereo baseline angles in the range of 15–25° for optimal topographic measurements. An off-nadir orientation of the spacecraft can be in conflict with the other on board experiments' requirements, so it has to be employed only for specific scheduled target.
HiRISE produces two types of Planetary Data System (PDS):

- Experimental Data Record (EDR), which are the permanent record of the imaging acquired by the instrument and successfully transmitted back to Earth. An EDR contains raw image and data and in a single HiRISE observation there may be up to 28 EDR files;
- Reduced Data Record (RDR), which have undergone radiometric correction and geometric processing to create map products associating a pixel to a latitude and longitude coordinate on the planet surface. RDR products are intended to be the most useful product for science data analysis and are those used for the analysis described in section 4.2.

4.1.2 MRO CTX

The Context Camera is on the Mars Reconnaissance Orbiter and provides context images for data acquired by other MRO instruments. It consists of a telescope with an aperture of 350 mm and a 5.7° field of view providing a 30-km-wide and ≥40-km-long swath from 290 km of altitude. The CCD detects in the band 500–700 nm and the spatial resolution is of ∼6 m/pixel (Malin et al., 2007). As of Planetary Data System (PDS) release 47 (December 2018, including data through May 2018), the instrument has returned over 100.000 images that cover 97.8% of the planet's surface (Robbins et al., 2019).

4.1.3 TGO CaSSIS

CaSSIS (Colour and Stereo Surface Imaging System) is the stereo imaging system on board the European Space Agency ExoMars Trace Gas Orbiter (TGO) (Thomas et al., 2017) that has been launched on 14th March 2016.
TGO is in a 400 km circular orbit with an inclination of 74°. This is not Sun-synchronous (unlike MRO), hence the spacecraft rotates through all local times of day several times per Mars season, having the unique ability to monitor how the surface colour and albedo changes with time of day as well as season. This orbit allows to monitor mid-latitudes, from -74° to +74°. CaSSIS provides images at a resolution of ∼4.6 m/pixel and, although the Context Imager (CTX) on MRO has a similar imaging scale, it does not provide colour images and useful stereo coverage is restricted to only ∼10% of Mars.
CaSSIS uses a single focal plane covered with a segmented filter and a rotation mechanism to acquire along-track stereo; multiple images are acquired in the along track direction providing sequences of overlapped images on the surface.
The spacecraft was designed such that one side is always nadir pointing. However, the spacecraft rotates about this axis in order to maintain sunlight orthogonal to the spacecraft solar panels. To compensate the rotation of the spacecraft and to accomplish also the requirement of acquiring stereo pair images, the telescope rotates around nadir axis and the spacecraft remains aligned to the ground-track motion.

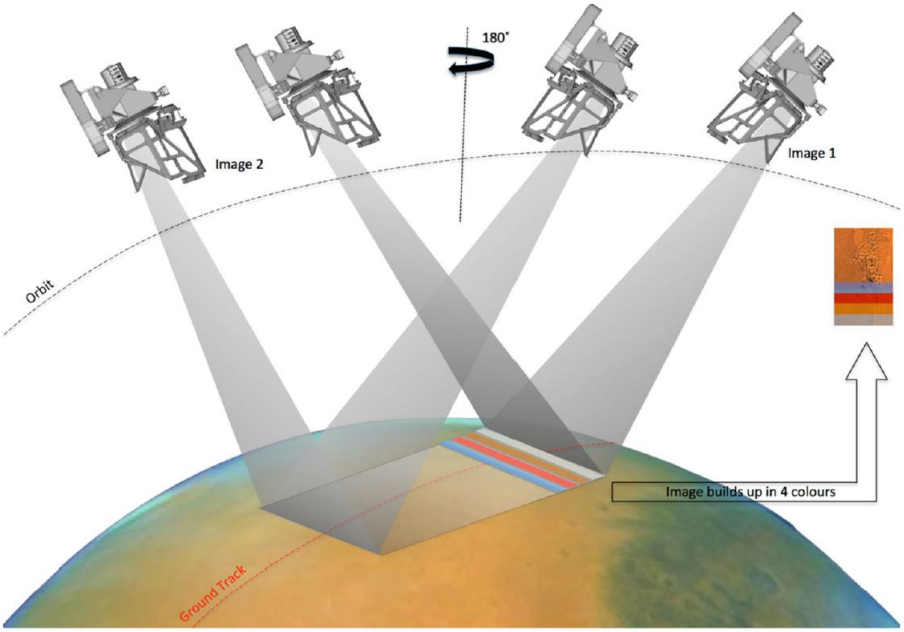

Figure 9: Rotation of the telescope during the acquisition of stereo pair images. The spacecraft moves from right to left. (Thomas et al., 2017)

The optical system consists of 4 aspheric mirrors and the telescope, which has an aperture of 135 mm and a focal length of 880 mm, is mounted on one side of the spacecraft and is tilted, together with the focal plane, by 10° with respect to the axis of symmetry of the bearing and rotates of 180° for the acquisition of an almost instantaneous stereo pair images (figure 9). The detector has been provided by ASI and INAF-OAPD and it is a spare model of SIMBIO-SYS, the instrument on board of the BepiColombo mission. It is a 2k × 2k hybrid Si-PIN based on the CMOS technology.

The wavelength bands for the four colour filters of CaSSIS were derived from the ones used on HiRISE (McEwen et al., 2007) and range from 400 nm to 1100 nm. The two first bands, BLU and PAN correspond closely to the first two bands used by HiRISE (BG and RED, respectively) ensuring consistency between the CaSSIS and HiRISE datasets. The two other CaSSIS filters, RED and NIR, split the third filter of HiRISE (NIR) in two. This additional colour is designed to improve the discrimination between expected surface minerals. As the reflectivity of the ice-free Martian surface at blue and green wavelengths is very low, the BLU filter provides an extremely high sensitivity to fog and surface frost or ice.

For courtesy of the CaSSIS team it was possible to exploit images and DTMs of selected locations.

4.1.4 MOLA

Mars Orbiter Laser Altimeter (MOLA) is an instrument on NASA's Mars Global Surveyor (MGS) spacecraft that was launched on November, 1996, and by March 9th, 1999, had slowly circularised to a Sun-synchronous, near-polar orbit with an average altitude of 378 km (Albee et al., 2001). MOLA determines the global topography of Mars by generating high-resolution topographic profiles. The instrument emits a

laser pulse of 1064 nm and measures the time interval that elapses from the emission to the detection of the signal reflection. Knowing the accurate velocity and location of the spacecraft it can be derived the distance from the surface. Pulses last 8.5 ns and are emitted at 100 ms intervals. The receiving optics is a Cassegrain telescope with a primary mirror of 0.5 m of diameter.
At the mapping altitude each laser spot illuminates a circle of diameter equals to 160 m on the surface with a spacing of ∼300 m (0.1 sec) per spot along the MGS nadir ground track, so the ground resolution is ∼460 m. The precision of the time-of-flight measurement is 2.5 ns, corresponding to an elevation of 37.5 cm, but the overall vertical uncertainty, considering also the radial-orbit error, is 3 m (Neumann et al., 2001). Thus, MOLA data, which globally cover Mars, provides a very good estimate of the altitude but with poor ground resolution.

4.2 Identification and location of lava tubes and skylights

The analysis was performed in ArcGIS, a geographic information system environment.
The region northern of Arsia Mons, the southernmost of the Tharsis volcanoes, has been chosen as area of interest because of the presence of a widespread network of collapsed lava tubes (figure 10)(Cushing, 2012).

Collapsed lava tubes sections in this region most likely belong to the overcrusted type because the visible lifted margins on the surface are a sign of their closeness to it and their widths are small (less than 100 m). It is possible to assert that these features have a volcanic origin because their sinuosity index (ratio between the collapsed lava tube trace length and the shortest path between starting and ending points) is much higher than 1, ruling out the tectonic origin of these features. In that case, fault traces and collapse pits related to dilatant/hybrid fracture opening are almost rectilinear.
The skylights opening on subsurface lava tubes voids and collapses distributed in chains can help to shed light in the internal characteristics related to pre-collapse conduits. One way to explore them is to measure parameters such as depth and width of the mapped collapses. Skylights and collapses can have different morphological characteristics that help to distinguish them from impact craters, -despite the common elliptic/round shape and flat or sloped bottom- such as the absence of lifted rims and ejecta and the presence of overhanging or vertical walls under which a lava tube cave can be hidden.

In CTX images the minimum dimension to recognise a feature and perform measurements of it is ∼24 m, considering the reasonable limit given by 4 pixels and the resolution of 6 m/pixels (section 4.1.2). For this reason it is difficult to recognise small deep pit craters, which are bowl-shaped and do not subtend underground voids and stable volumes in the subsurface, from skylight-like depressions. However, shallow pit craters were identifiable in certain condition of illumination from the fuzziness of the shadow edge and excluded from the analysis.
Single images of skylights and lava tubes were downloaded to perform their analysis. To know which image covered a specific region without downloading a useless amount of data, footprints of CTX and HiRISE images were downloaded in a shapefile format from "`https://ode.rsl.wustl.edu/mars/coverage/ODE_Mars_`

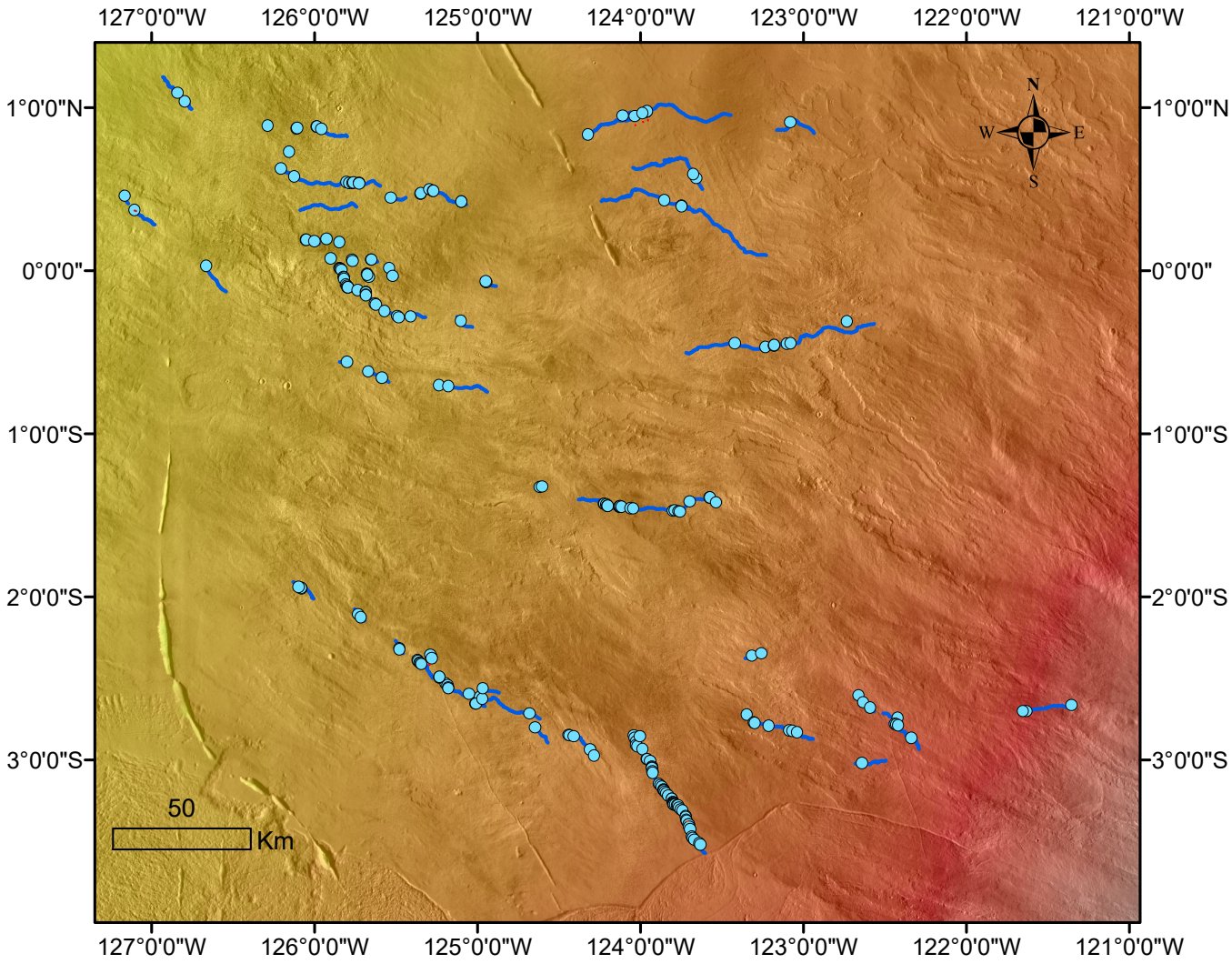

Figure 10: Area of interest at North of Arsia Mons: dots are skylights, lines are the interpreted lava tube path according to skylights alignments.

shapefile.html". Footprints were imported in the ArcGIS project and it was used the spatial join tool to identify which image contained the target. In many cases there were more than one image. CTX images were downloaded from "https://viewer.mars.asu.edu/viewer/ctx#T=" as pyramidized TIFF, while HiRISE from "https://hirise.lpl.arizona.edu/" in JP2 format. Some images were not georeferenced, so it was necessary to georeference them using control points. They must be inserted manually on the image that has to be georeferenced and then linked to the same features on the reference map. They have to be chosen in different areas of the image, thus avoiding the collinearity, and on features recognisable in the base map. Subsequently, the software warps and adapts the image to the base map with a second degree polynomial transformation and inserts a reference system in the image metadata.
Paths of the possible lava tubes were interpreted using as markers the aligned skylights and the orientation of their elongation to understand the possible direction of the principal conduit. In fact, minor axis of collapses of the same structure does not vary because it depends on the width of the structure, while the major axis can continue to expand on the length of the conduit (Sauro et al., 2018).
Sinuosity and average slope of the interpreted lava tubes paths were estimated with the software "Stream Gradient and Sinuosity Toolbox for ArcGIS", which calculates the sinuosity as the ratio between the lava tube length and straight line distance between the starting and ending points of the lava tube. Therefore sinuosity equals 1 for straight lava tubes and has higher values for lava tubes with many curves. The average slope is calculated with eq. 1, using MOLA data as Digital Terrain Model (DTM) to obtain the difference in height ("*rise*") between the starting and ending points of the lava tubes, whose distance on the ground is called "*run*".

$$Slope = \arctan\left(\frac{rise}{run}\right) \tag{1}$$

In some cases DTMs at higher resolution were generated from CaSSIS and HiRISE stereo pair images, and it was possible to measure with higher accuracy the slope of some lava tubes. Resolutions of these DTMs depend on the characteristics of the starting images and were produced with a ground resolution equals to that of the starting images and the vertical one of 0.2 m for HiRISE images and 4 m for CaSSIS images.
Skylights were mapped on the CTX image mosaic with overlaid HiRISE images, where available, by tracing the perimeter of each one of them and then, using the Minimum Bounding Geometry tool, the shape of the skylight was approximated to a rectangle and width and length were extracted. The width of skylights are representative of the width of the underlying lava tube; in fact, skylights which have an elliptical perimeter, so an aspect ratio greater than one, can form from a collapse that enlarges with time and that can reach a maximum width, which is that of the lava tube.
An estimate of the minimum depth of the skylights was provided by combining in trigonometric equations the measurement of the shadow inside the skylight, the known position of the spacecraft and the Sun direction (Cushing et al., 2015). A simplification of the system is depicted in figure 11, including the incidence angle i of the Sun and the emission angle e of the spacecraft with respect to the normal to the surface.

Defining the phase angle φ as the angle between the Sun and the spacecraft and considering an eastward illumination of the Sun, it is possible to distinguish between an eastward ($\varphi = i - e$) or westward ($\varphi = i + e$) orientation of the spacecraft, described respectively in figure 11A and 11B. In both cases the observed shadow is marked with D'_s and the depth of the skylights as d_s.
In figure 11A it can be observed that part of the shadow (D_N) is not visible from the spacecraft. So, in the case $\varphi = i - e$, the value of the depth is:

$$d_s = \frac{D_N}{tan(e)} \tag{2}$$

but the value of D_N cannot be measured, so, considering that d_s can be described also by:

$$d_s = \frac{D_N + D_s}{tan(i)} \tag{3}$$

a value for D_N can be found in eq. 5 obtained combining equations 2 and 3.

$$\frac{D_N}{tan(e)} = \frac{D_N + D_s}{tan(i)} \tag{4}$$

$$D_N = \frac{D_s tan(e)}{tan(i) - tan(e)} \tag{5}$$

Considering that the spacecraft does not perform exactly nadir observations, the emission angle e must be taken into account, so the observed dimension is $D'_s = D_s cos(e)$. Then, equation 2 becomes:

$$d_s = \frac{D'_s}{cos(e)(tan(i) - tan(e))} \qquad for \quad \varphi = i - e \tag{6}$$

For the case $\varphi = i + e$, with reference to figure 11B, depth can be expressed by:

$$d_s = Scos(i) \tag{7}$$

where $S = \frac{D'_s}{cos(\Theta)}$. Given $\Theta = \pi/2 - (i + e)$, the depth is:

$$d_s = \frac{D'_s cos(i)}{sin(i + e)} \qquad for \quad \varphi = i + e \tag{8}$$

Inclination, emission and phase angles are information contained in the label of every image and depend on the conditions during the observations.
To make automatic the calculation and the differentiation of the two cases a Python script was realised.
The measurement of D'_s was performed using also another information contained in the label of the images and related to the direction from which the light is coming: the subsolar azimuth. It is an angle defined using the position of the subsolar point during the observation, i.e. the longitude and latitude of the point in which the solar rays are perpendicular to the planet surface. The subsolar azimuth is the

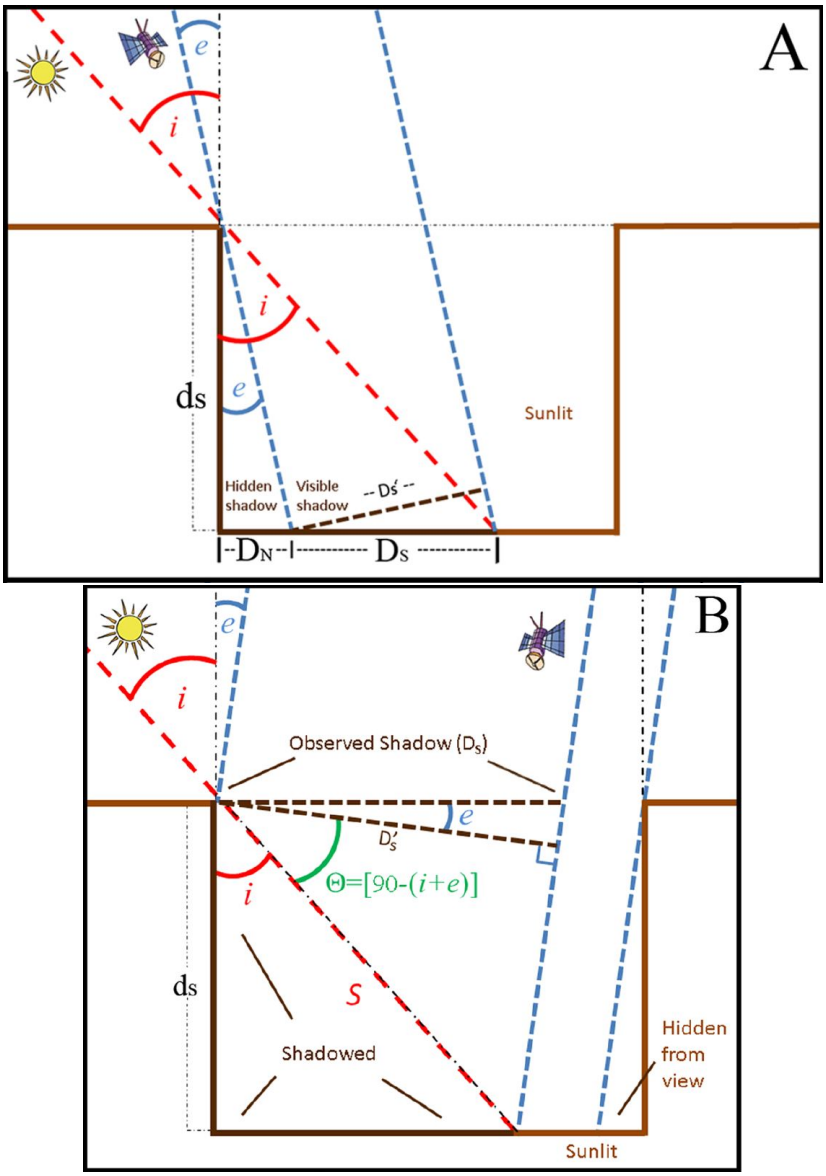

Figure 11: Scheme section of a skylight (Cushing et al., 2015). i and e are the incidence and emission angles, defined from the zenith, d_s is the measured depth of the skylight and D'_s is the apparent length of the shadow as seen from the spacecraft. (A) depicts the case $\varphi = i - e$, in (B) is portrayed the case $\varphi = i + e$.

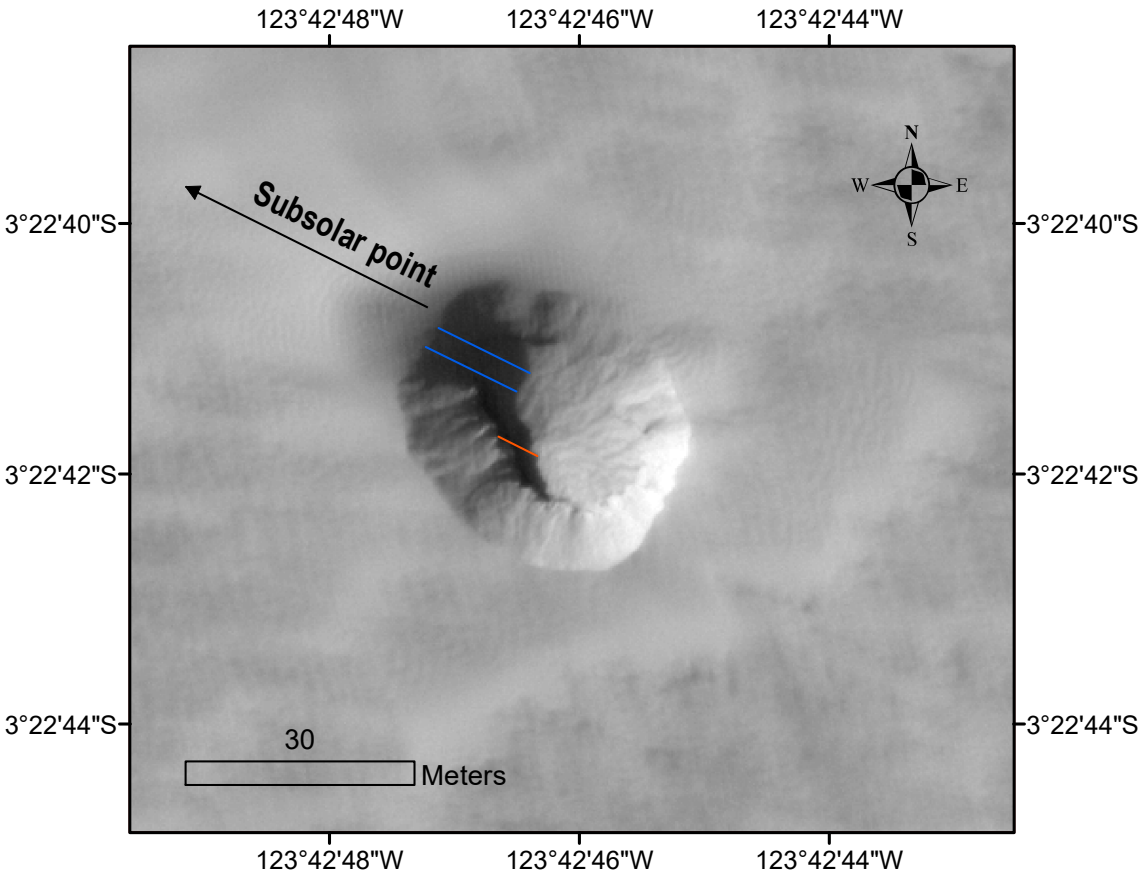

Figure 12: Detail of the skylight S52 in HiRISE image: ESP_017901_1765. Lines are drawn in direction of the subsolar point. For this skylights depth was measured in three points: blue lines allow to measure the depth directly from the ground level, while using the red line it is necessary to add the height of the slope.

angle clockwise from the reference axis of the observation (a line from the centre to the right edge of the image footprint considered) to the direction to the subsolar point on the target body. So, for every image, a line connecting the subsolar point to the centre of the image was drawn and D'_s was measured as the distance from the shadow casting rim to the shadow cast in the direction of the drawn line (figure 12). It follows that the resulting measurements gives an estimate of the height from the rim to its shadow cast on the bottom of the skylight or, if the shadow is too long that the bottom cannot be seen, it can be determined a minimum depth.

In cases in which the shadow began at the inner and lower edge of the rim, as marked by the red line in figure 12, the height from the surface to the end of the slope had to be added to the measured depth. The inclination of the slope was assumed to be an angle of repose of $\alpha = 35°$, which is a value that can be found on Earth considering that the angle of repose depends only on the material and not on gravitational acceleration (Atwood-Stone and McEwen, 2013, Melosh, 2011). Also

for these measurements two cases were discerned, and similar considerations to the previous ones lead to the following results:

$$h = \frac{D'_s sin(\alpha)}{sin(\gamma)} \qquad for \quad \varphi = i - e \tag{9}$$

$$h = \frac{D'_s sin(\alpha)}{cos(\gamma)} \qquad for \quad \varphi = i + e \tag{10}$$

with $\gamma = \pi/2 - \alpha - e$.
The shadow length measurements were made assuming that the direction of the spacecraft roll was parallel to the subsolar azimuth, which is a reasonable approximation because both lie on East-West direction in non polar latitude and a small angle between these two directions do not change much the result (Cushing et al., 2015).
These methods were applied also to skylights around Arsia Mons, making a selection of those with a possible volcanic origin.
In few cases it was possible to have the Digital Terrain Model of the skylights, from which very reliable measurements of depths were obtained, providing a term of comparison with the results obtained with the previous method and thus performing an evaluation of its accuracy.

4.3 Measurement of Terrestrial skylights

Terrestrial skylights were considered to perform a comparison with Martian skylights dimensions. Measurements were made on a lava tube with similar characteristics of the Martian ones considered here, so with an overcrusted origin. For this reason Kazumura cave in Hawaii was chosen as term of comparison as one of the well-known Mars analogues in terms of style of volcanism, emplacement processes and surface morphologies. The total length of this cave is 65.6 km with a vertical extent of 1101.8 m. The average slope is 1.9° over a straight line distance of 32.1 km, which makes Kazumura cave the longest linear cave in the world. This distance can be traversed all underground by walking 41.8 km (Allred and Allred, 1997).
Measurements on skylights were performed on the Kazumura Cave Atlas, which was produced from a speleological survey (Allred and Allred, 2002).
To perform the comparison, the height and width of the Terrestrial skylights were measured as if they were observed from a satellite. For this reason the depths were measured from the rim to the debris deposits (see figure 13) and the considered width was the minimum dimension of the skylights visible from the surface. Measurements also on the real dimensions of the lava tube were performed to produce an estimate of the asymmetry ratio (Sauro et al., 2018).

4.4 Estimate of the yield strength

Lava can be considered to behave as a Bingham fluid, a non-Newtonian fluid that begins to deform permanently when a sufficiently intense force is applied on it (Shaw, 1969). Observations show lava flows which cease with high flow fronts lying on slopes and without the presence of topographic features. Moreover, they acquire fixed depth and width soon after the start of the activity. An ideal Newtonian fluid

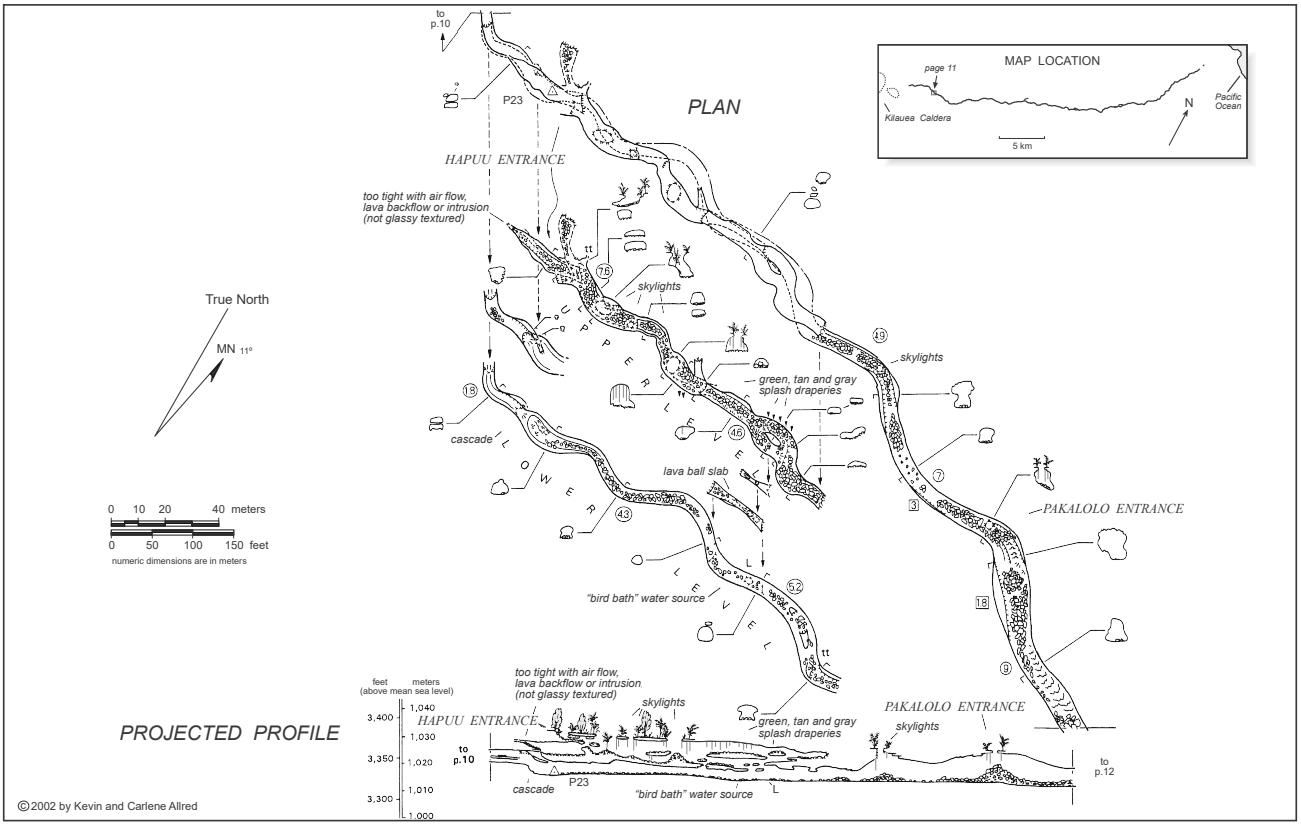

Figure 13: Example of page of the Kazumura cave Atlas containing five skylights, whose widths were measured on the plan and depths on the projected profile. *Image courtesy of Kevin and Carlene Allred.*

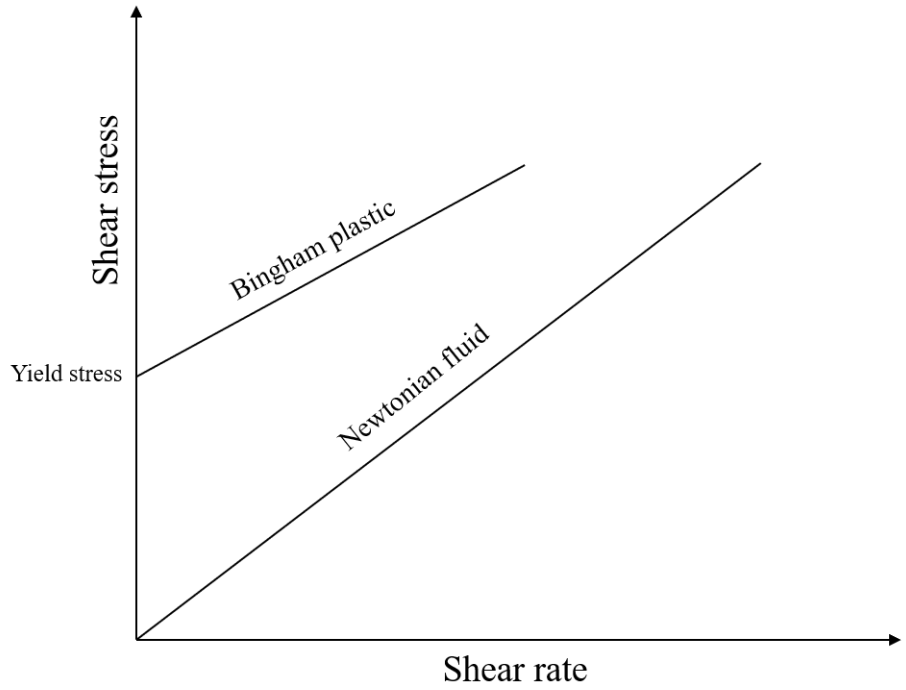

Figure 14: Bingham plastic and Newtonian shear stress. Bingham fluids begin to deform (shear rate > 0) when a stress higher than the yield stress is applied.

would continue to flow and spread laterally until it was restricted by topography or until surface tension prevented streaming when it would be extremely thin (Hulme, 1982). The minimum stress to be applied to lava for having a non null shear rate is the yield strength. A comparison between the behaviour of Bingham plastics and Newtonian fluids is shown in figure 14.

The shear stress of a Newtonian viscous fluid can be described by:

$$\tau_N = \eta \frac{\partial u}{\partial y} \tag{11}$$

with u velocity of the fluid, y the height of the fluid and η viscosity, while the shear stress of a Bingham fluid is:

$$\tau = \tau_y + \eta \frac{\partial u}{\partial y} \tag{12}$$

where τ_y is the yield strength. Using this assumption, and considering gravity and shear stress as the only acting forces, it is expected that lava flows stop at a critical slope or thickness when the value of the shear stress becomes less than τ_y and consequently the geometry of the flow is recorded in the solid form, creating a relation between the geometry of the flow and the yield strength.
The estimate of the yield strength was performed for three cases in which the only acting forces are gravity and shear stress but differs each other from assumptions related to the origin and evolution of lava tubes. In the first case lava was assumed to flow freely and in laminar fashion on an inclined terrain, leaving a drained tunnel. The equilibrium condition of the flow is described by equation 13 (Hulme, 1974), given $g = 3.711$ m/s^2 the gravitational acceleration of Mars and $\rho = 2750$ kg/cm^3

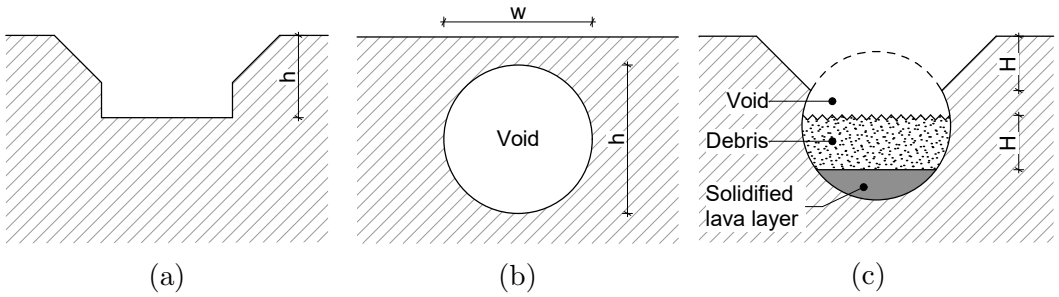

Figure 15: Section of models of lava tubes used to estimate (a) τ_1, (b) τ_2, (c) τ_3.

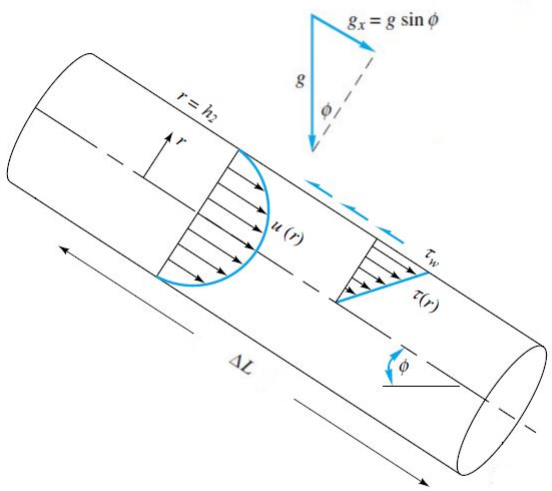

Figure 16: Flow of a Bingham fluid in a circular tube. (Modified from White (2011))

the density of basaltic Martian lava flow, which is usually a value between 2500 and 3000 kg/cm^3.

$$\tau_1 = \rho g h_1 sin(\phi) \tag{13}$$

The height h_1 of the lava flow was considered to be the measured depth of the skylights shown in table 8, that include the present void and the thickness of the collapsed roof (figure 15a). The inclination ϕ of the terrain was that measured for lava tubes described in section 4.2.

The second estimate of yield strength was realised considering flows that during the activity filled tubes with circular section, and afterwards left the tubes drained (Honda, 2018). With reference to image 16, the condition of equilibrium is expressed by equation 14, which leads to the estimate of the yield strength (equation 15).

$$\rho g \Delta L \pi \left(\frac{h_2}{2}\right)^2 sin\phi = \tau_y 2\pi \frac{h_2}{2} \Delta L \tag{14}$$

$$\tau_2 = \rho g sin\phi \frac{h_2}{4} \tag{15}$$

In this case the section of the tube was assumed to be circular, according to the properties of overcrusted lava tubes; this means that depths of the lava tubes equal their widths (asymmetry ratio equals 1), so the height h_2 in this equation is the measured width of the skylights listed in table 8, which are representative of the lava tube width (figure 15b). Since the first two models assume drained lava tubes, the values τ_1 and τ_2 are an upper limit to the real value of yield strength.
In the third case lava tubes sections were approximated to be circular too, but lava did not fill the tubes, so the equilibrium condition is that expressed by equation 13. Moreover, it was made the assumption that the bottom of the skylight is filled with debris and that the tube was not fully drained, but there is still a layer of solidified lava, whose thickness is the value that was used as height h_3 in the equation of equilibrium. The estimate of the thickness of lava was performed assuming that the debris was made only of material of the collapsed roof and that the height of the lava tube equals the width w of the skylight (figure 15c). In the expression 16 is shown how h_3 was estimated, with w the measured width of the skylight, which was used as height of the lava tube, d the measured depth of the skylight and H the thickness of the roof used here as thickness of the debris at the bottom of the lava tube.

$$h_3 = w - d - H \tag{16}$$

The distance from the top of the lava tube to the terrain above cannot be estimated, but for lava tubes near the surface it can be neglected. The value of H was estimated assuming that the thickness of the roof is the vertical distance between the terrain and the internal rim in skylights similar to that shown in figure 12, and it was calculated with expressions 9 or 10. These measurements could be performed only on HiRISE images, so for the third case the sample is smaller than the other two cases.

4.5 Digital Terrain Models from stereo pair images

Three dimensional reconstructions of specific locations on the surface of Mars were performed in order to have a term of comparison for evaluating the accuracy of the measurements of depths obtained with the length of the shadows and for estimating the inclination of the terrain using spatial resolution better than that of MOLA data. In fact, even though laser altimetry has an almost global coverage, it suffers from poor spatial resolution and positional errors.
Digital terrain models from stereo pair images presented in this thesis were realised by Dr. Cristina Re from INAF - Astronomical Observatory of Padova.
The construction of a DTM from stereo pair images requires the acquisition of the same area from different points of view to create a parallax effect on the image, so that the same object feature has different locations in distinct images. Accuracy of the stereo reconstruction is defined by the baselength and the stereo-angle, which depends on the camera configuration. In order to produce stereo pair images, the setting of the cameras on board an orbiter can be composed of two different cameras that are tilted of a stereo angle and offer a wide field of view, or of a single camera that observes the same area with different points of view in two distinct moments.
HiRISE is composed of one camera that covers $\sim$0.1 % of the surface of the planet with stereo pairs (McEwen et al., 2007). This camera works in the push-broom

mode, so that captures images one scan line at a time, building up an image over the course of several seconds as the satellite moves through the sky. For the creation of stereo pairs the spacecraft is tilted in consecutive orbits.
EDR are used by the Integrated System for Imagers and Spectrometers (ISIS) which performs the photogrammetric pipeline initialization for the creation of the DTM. The steps followed by ISIS are (Re et al., 2012):

- the radiometric calibration, whose product is an image as if it was produced from a nominal camera system;
- the channel stitching, that consists of combining two HiRISE channels to form a single CCD image;
- the projection of EDR image into ground coordinates (latitude and longitude) and then back into the image coordinates of an idealized, distortionless camera; then, it is obtained the relative offsets between CCDs, which are mosaicked together;
- the map projection of the images, eliminating some of the perspective differences in the image pair that are due to large terrain features. The resulting image pairs have only small perspective differences in the images, which are exactly the features that the stereo correlation process has to detect. Then it is produced the orthorectified image, i.e. projected onto the reference surface of the Mars spheroid.

Subsequently, the Ames Stereo Pipeline (ASP), developed by the NASA AMES Research Center (Beyer et al., 2018), performs the space intersection (triangulation) to compute the 3D point coordinates. Knowing the interior parameters, that characterise the camera system (focal length, sensor size and principal point position), and exterior parameters, which define the position and the attitude of the camera during the acquisition with respect to a known world reference frame, the locations of the 3D points on the surface of the planet can be evaluated from measurements of the space coordinates (x1,y1) and (x2,y2) in the two stereo pair images of the homologous features.
The creation of 3D reconstructions from CaSSIS images was preformed with the 3DPD software (three-Dimensional reconstruction of Planetary Data) developed at INAF - Astronomical Observatory of Padova (Simioni et al., 2017).
Data were acquired by the camera with a push-frame mode, which consists of taking images (framelets) partially overlapped in order to reconstruct a final swath. After the acquisition of the first image, the telescope, and not the entire spacecraft, rotates of 180° and captures the second image of the stereo pair; this approach guarantees a sufficient baseline to reach a vertical precision equal to the pixel on-ground (Thomas et al., 2017).
The full pipeline of the software (Simioni et al., 2018) includes the geometrical distortion calibration, the mosaicking of the images on the MOLA quote, the definition of tie-points (recognition of the same feature in the two images) and a Least Squares Matching algorithm provides a dense matching point cloud then interpolated on a regular grid for the DTM generation with a fixed ground sample distance (GSD) of 4.6 m: the same spatial resolution of the starting images.

5 Results

In table 7 are listed the identified lava tubes in the region at north of Arsia Mons with their properties. Usually lava tubes do not exhibit features on the surface, but overcrusted ones are often near it and, as in this case, show their lifted margins which allow to detect the paths of the flows. Their presence can also be guessed by the detection of collapses, which provided information for estimating the length and width of lava tubes. The average slope in table 7 is calculated with the "Stream Gradient and Sinuosity Toolbox for ArcGIS" using MOLA data as DTM. The standard deviation of the slope was evaluated from the propagation of error calculated on the equation 1, considering the ground and vertical resolution of the DTM as the error on *run* and *rise* variables, respectively (see section 4.1.4).
In table 7 is also given the number of detected skylights that lie on each lava tube and the estimated length of the lava tubes, some of which are longer than Kazumura cave.
It is possible to compare the slopes of lava tubes obtained by DTM produced with CaSSIS or HiRISE stereo pair images and MOLA data. In these cases the 3D Analyst tool was used to obtain the profile of the height of the piece of lava tube included in the image, and the same portion of lava tube was analysed with MOLA data with the same method. From the profile of the lava tube *rise* and *run* estimates were extracted and the slope was estimated with equation 1. Results for the lava tubes to which was possible estimate the slope with two different DTMs are described in table 1 and an example of profile is shown in figure 17.

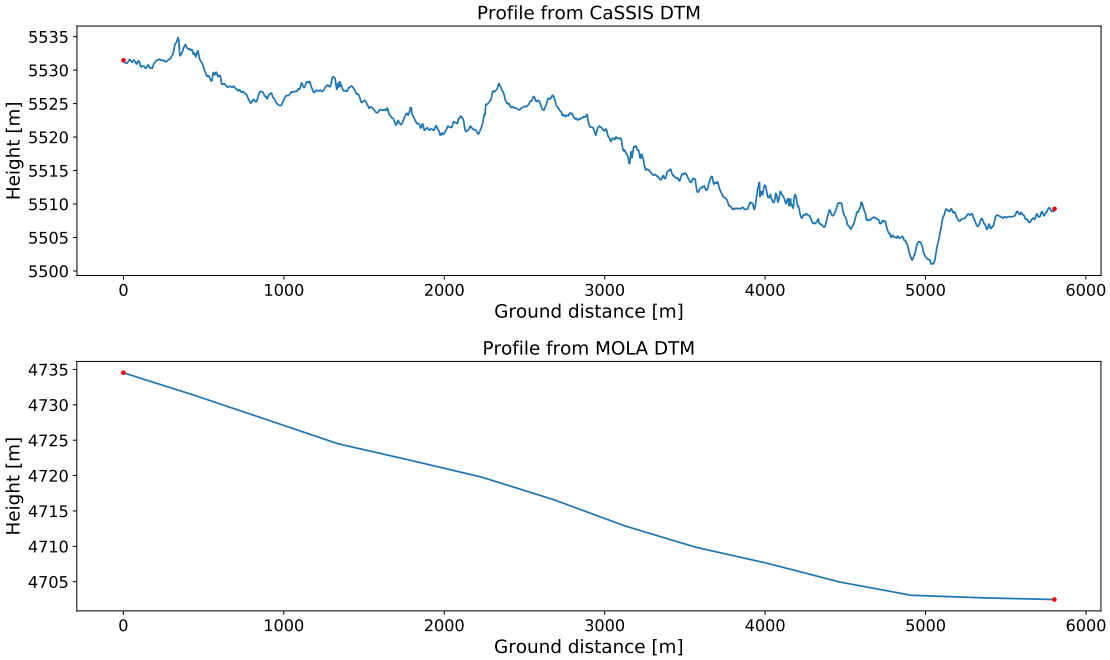

Figure 17: Profile of the portion of L0 included in the DTM generated from CaSSIS stereo pair images (top) and MOLA (bottom). Red dots mark the points from which *rise* and *run* were evaluated.

The estimate of the uncertainties in the measurements was performed considering as errors of *rise* and *run* the values of vertical and ground resolution: for both

Name	Slope HiRISE DTM	Slope CaSSIS DTM	Slope MOLA DTM
L0	/	0.219 ± 0.039	0.316 ± 0.039
L3	/	0.468 ± 0.072	0.386 ± 0.076
L40	0.536 ± 0.003	/	0.473 ± 0.068

Table 1: Comparison between slopes of the same portion of lava tubes obtained by different DTMs.

CaSSIS DTMs the vertical resolution is 4 m and the ground resolution is 4.6 m, while the HiRISE DTM has vertical resolution of 0.2 m and ground resolution of 0.5 m. The error on the slope was obtained propagating the uncertainties of *rise* and *run*.
As can be seen from table 1, the slope of the terrain measured with different DTMs for L3 and L40 are comparable within their uncertainties, while the estimates of the slope for L0 agree within 2σ. Thus, the slopes measured for every lava tube can be considered a good estimated of the real ones.

In the region at north of Arsia Mons were detected 193 skylights. Their coordinates and characteristics are listed in table 8.
The majority of these skylights were observed with CTX and, as resulting from table, they are small features compared to the resolution of the instrument. For this reason some of their characteristics were not detectable and it is possible that some of them are more similar to elliptical pit craters, but they are surely structures that were formed by the presence of some kind of void in the subsurface, so they are at least representative of the width of the lava tube and of a minimum depth. Detection of these skylights with higher resolution images, such as those of HiRISE, would clarify their properties.
The errors on skylights depth were estimated assuming that the uncertainty was given by the dimension of the pixels projected considering the emission and phase angles, as in equations 2 and 3. Pixels dimension of CTX images was assumed to be 6 m, while for HiRISE images was considered an error given by two pixels of 0.25 m each. This estimate was performed considering that the resolution of HiRISE images varies between 0.25 and 0.50 m/pixels and because for the operator is more difficult to choose the points that mark the begin and end of the shadow. The image resolution gives an estimate of the error also for the width, and is assumed to be 6 m for CTX images and 0.50 m for HiRISE images.
Since skylights are small related to the resolution of CTX images, it was performed a comparison between the depth measured from HiRISE and CTX images of those 32 skylights for which it was possible. From the results, shown in figure 18, can be observed that usually the depth measured on CTX images is overestimated compared to that from HiRISE images, but it can be concluded that in most of the cases the depth agrees within 2σ.

In order to verify the validity of the measurement of depths obtained exploiting the length of the shadows, it was made a comparison with depths obtained with DTMs generated from stereo pair images of CTX or HiRISE. In the region considered at North of Arsia Mons it was possible to perform only measurements of the depth of the skylight S166, which was obtained from a DTM generated with stereo pair

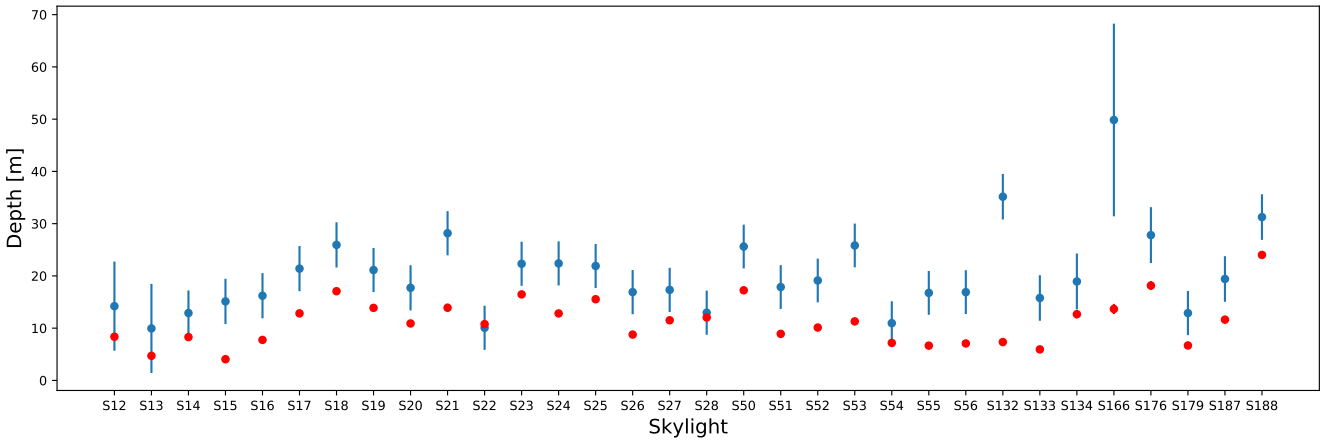

Figure 18: Comparison between measured depth of skylights on HiRISE images (red) and CTX images (blue).

Skylight	Longitude	Latitude	Shadow depth [m]	DTM depth [m]	Images
S166	-127.10	0.37	13.67 ± 0.97	6.63 ± 0.28	ESP_049021_1805 ESP_049298_1805
/	-119.98	-13.84	64.99 ± 0.26	54.65 ± 0.28	ESP_033342_1660 ESP_050089_1660
/	-123.93	-13.95	46.68 ± 0.55	55.81 ± 5.66	MY34_005151_345_1 MY34_005151_345_2

Table 2: Comparison between depths measured exploiting the length of the shadow and obtained from a DTM. In the column *Images* are listed the stereo pair images used to generate DTM.

images of HiRISE. The other DTMs created in this area were from stereo pair images of CaSSIS and their lower resolution did not allow the detection of the skylights. For this reason other skylights were considered, and, since their analysis is only employed to verify the method used previously for the estimate of depths, it was not taken into account their origin but only the detectability of their depths from DTMs. Two skylights were detected as useful at South of Arsia Mons and one was analysed on a CaSSIS DTM and the other on an HiRISE DTM. An example of DTM of skylight and its front section is presented in figure 19.

The uncertainty of the depths were estimated from the vertical resolution of DTMs and applied to the identification point of the rim and of the bottom of the skylight. In table 2 there are the results of the depths estimated from the length of the shadows and from DTMs.

Both methods have small uncertainties due to the very high resolution of the images and measurements do not agree. A problem could arise from the place where the depth in the DTM was measured that did not match exactly the end of the shadow. Despite the disagreement of the two methods, for the following analysis all estimates of depths obtained with the length of the shadow cast were considered.

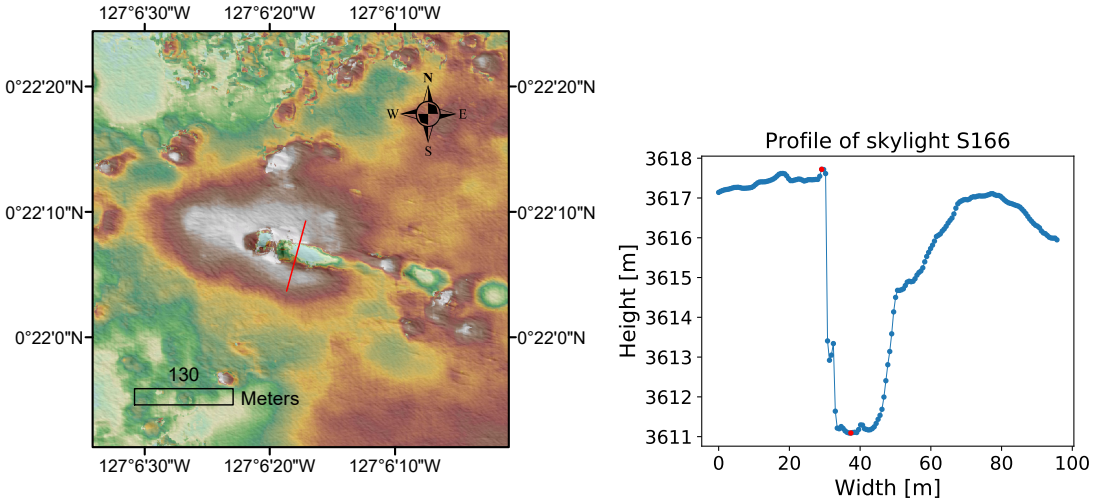

Figure 19: DTM generated from HiRISE images ESP_049021_1805 and ESP_049298_1805 and profile of skylight S166 extracted in correspondence of the red line marked in the DTM.

Although, it must be taken into account that the instrumental uncertainty considered to estimate the errors on the measurements of the shadows, and therefore of the depths, are the minimum uncertainty related to the measurements and do not include errors due to the employed method because they cannot be evaluated. In fact, during the measurements emerged that resolution was not the only factor that improved the estimate; thus, in some cases, different CTX images of equal resolution of the same skylight gave different results on the depth, probably because of other illumination conditions and angle of observation.

5.1 Comparison between Martian and Terrestrial skylights

In order to compare the minimum depth and width of Martian and Terrestrial skylights, it was increased the sample of Mars skylights analysed, including also some features having a possible volcanic origin in the South region of Arsia Mons. In table 9 there are the coordinates of the used skylights with the estimate of depth and width calculated using the length of the shadows or exploiting the measurements found in literature (Cushing et al., 2015).

Figure 20 shows that Terrestrial skylights are smaller than the Martian ones, but this is not caused by the limited resolution of the images of Mars because in HiRISE images, which have resolution of 25 cm/pixel, skylights of dimension less than 10 m should be detectable. Bigger Martian volcanic structures are expected considering the value of the gravitational acceleration on Mars, which is 38% of the Terrestrial one (see section 2.2). A linear model do not describe well these data because the value of the coefficient of determination R^2 is $\simeq$0.70, so not enough near the value of 1. This applies also considering only measurements on Martian skylights performed on HiRISE images (see figure 20b), which give a better estimate of depth and width.

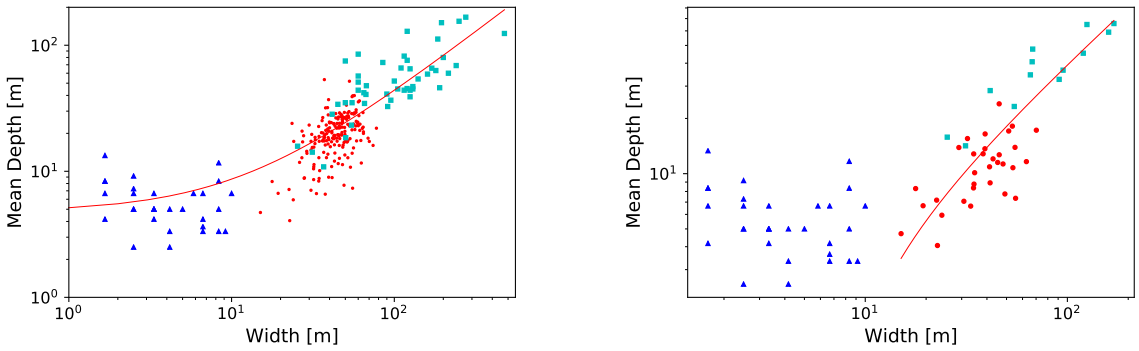

(a) m = 0.39, q = 4.74, $R^2 = 0.67$ (b) m = 0.42, q = -2.85, $R^2 = 0.74$

Figure 20: Width to depth plots of considered skylights on Earth (blue triangles), on Mars at north of Arsia Mons (red dots) and around Arsia Mons (cyan squares). In (b) were plotted only Martian skylights measured on HiRISE images. Values of the linear fit $y = mx + q$ are shown below the corresponding plot plot.

Set of skylights	d/w
E	1.882 ± 0.2
M	0.465 ± 0.009
MH	0.352 ± 0.002
MN	0.464 ± 0.011
MNH	0.295 ± 0.003

Table 3: Mean values of the asymmetry ratio calculated on skylights observed on Earth (E), Mars (M), Mars on HiRISE images (MH), Mars at North of Arsia Mons (MN), Mars at North of Arsia Mons on HiRISE images (MNH).

At least, for Martian skylights on overcrusted tubes, it is possible to observe that the depths tend to increase with the widths.
For every set of skylights it is possible to measure the asymmetry ratio, which gives an estimate of the shape and ellipticity of lava tubes section. Results are presented in table 3, where the errors of the mean values were calculated as:

$$\sigma_{\bar{x}} = \sqrt{\frac{\sum_i \sigma_{x_i}^2}{N^2}} \tag{17}$$

in which σ_{x_i} is the uncertainty of the asymmetry ratio calculated for each skylight that was obtained with the propagation of errors on the depth and width. The errors on the width were derived from the resolution of the images.

It can be observed that Terrestrial skylights are deeper than wider, while Martian skylights are wider than deeper. The ellipticity of the section of Martian lava tubes can be a result of the filling by the debris of the fallen roof and by sand transported by eolian processes.
Considering the internal dimensions of Kazumura cave lava tube, the value of the asymmetry ratio is 0.95 ± 0.04. This result is in favour of the fact that overcrusted lava tubes have a circular section (see section 2.3) and that the depths and widths that can be detected from orbital images are only a measurement of the

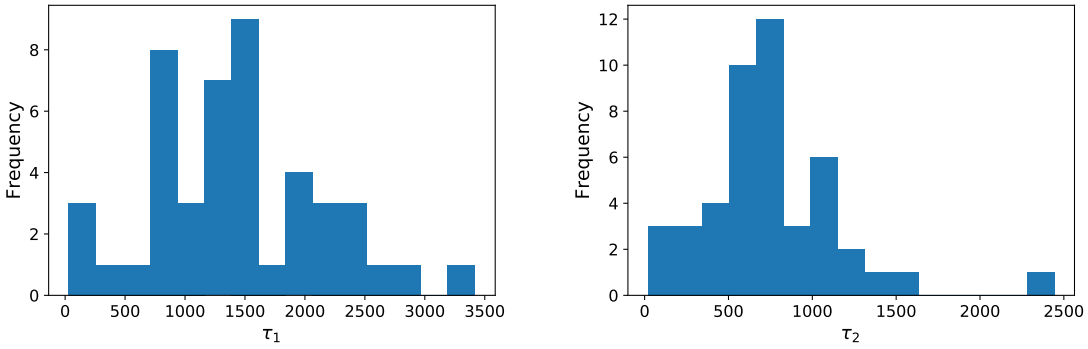

(a) (b)

Figure 21: Histograms of values of τ_1 (a) and τ_2 (b) averaged on lava tubes.

void currently observable and are not representative of the real dimensions of these structures. Measuring the internal dimensions of Kazumura cave larger depths are obtained because debris at the bottom of the lava tube are not considered, and in some cases also the width is larger than the minimum width of the skylight because the collapse of the lava tube occurred in a point where the section of the lava tube widens due to lava falls or intersections between the tunnels.

5.2 Yield strength

The value of the yield strength related to lava flows was estimated for each skylight and the associated uncertainty was calculated according to the propagation of errors applied to each expression for τ. It can be assumed that Martian lava, as the Terrestrial one, is composed of basaltic material, but it can have a variable density depending on different factors, including their composition (rich or poor in silica), pressure, temperature and water content. For this reason the range of values of ρ is generally between 2500 and 3000 kg/m^3, so it was assumed the value of $\rho = 2750 \pm 250$ kg/m^3. The slopes ϕ of lava tubes are shown in table 7. In equation 13 an other variable subjected to uncertainty is h_1, which is assumed to be the measured depth of skylights indicated in table 8. For the estimate of τ_2 it was used the width of the skylight as height, because of the assumption of circular section lava tube; its error is related to the resolution of the images. The error on h_3 is given by the square root of the sum of squared errors of every variable composing h_3: the width of the skylights as height of lava tube, for the assumption of circular tube, the measured depth of the skylights and the thickness of the roof H. The error on H was estimated from the propagation of errors of equations 9 or 10.
Assuming a major event forming each lava tube, it can be assumed only one value of yield strength for each lava tube. For this reason the values of τ_1, τ_2 and τ_3 were averaged for each lava tube. The distribution of τ_1 and τ_2 are shown in figure 21. Histogram of τ_3 was not realised because it was estimated only for the 25 skylights, that were observable in HiRISE images, related to four lava tubes. Results of τ_3 averaged on the four lava tubes are shown in table 4.

In table 5 values of τ_1, τ_2 and τ_3, averaged on the results obtained for each lava tube, are shown and they can be compared to values of τ that were estimated by

Lava tube	τ_3 [Pa]
L0	1286.19 ± 60.43
L9	1351.84 ± 12.42
L40	4258.65 ± 11.63
L46	101.42 ± 9.15

Table 4: Estimates of τ_3 averaged on lava tubes.

τ_1 [Pa]	τ_2 [Pa]	τ_3 [Pa]
1425.78 ± 7.45	742.62 ± 2.78	1749.52 ± 15.86

Table 5: Mean values of the yield stress for the three models.

Hiesinger et al. (2015), which for Arsia Mons are $2.54 \cdot 10^2$ Pa$< \tau < 9.63 \cdot 10^3$ Pa. These values were estimated using a different method: it was used the thickness of solidified lava flows on the surface as height.
The mean values found with all the three methods are included in the mentioned range and compatible with a lava of basaltic composition. Since τ_1 and τ_2 are an upper limit to the value of yield strength, their estimates should be larger than τ_3. The discrepancy with the expected result can be explained by not having considered possible sedimentation of sand caused by eolian processes. In this case the value of H in equation 16 results underestimated, thus h_3 should be smaller, leading to a smaller value of τ_3; while the value of h_1 in equation 13 is underestimated, producing an underestimated value of τ_1.

For the analysed area it was possible to estimate the values of τ using the slope obtained from a DTM generated from CaSSIS stereo pair images and perform a comparison with results of MOLA data in the same region. The DTM considered covers a portion of the lava tube L0 on which lie four skylights observable on HiRISE image ESP_017901_1765. Two of these skylights show a measurable roof thickness, so it was possible also to evaluate τ_3. Results are shown in table 6, and estimates for τ_1 and τ_2 are compatible within 1σ, and τ_3 within 2σ.

Surely these models, with their assumptions, introduce uncertainties in the evaluation of the yield strength and this can be seen from the different values in the three cases and also from the distribution of these values. But yield strength is a property of lava and depends on many factors, such as the silica and water content of lava and pressure and temperature conditions, so finding different values of τ in different lava tubes can be also an indicator of different properties of the lava.
Every model has some weaknesses:

- The first model considers a drained tube in which free lava flowed. Following the reasoning made in section 4.4, forces acting on the flow were so strong that lava didn't solidified in the lava tube, so the value of τ_1 should be higher than

	τ_1 [Pa]	τ_2 [Pa]	τ_3 [Pa]
MOLA	453.71 ± 76.44	474.11 ± 76.36	1108.08 ± 138.32
CaSSIS	313.94 ± 67.93	328.06 ± 69.37	766.72 ± 123.16

Table 6: Mean values of the yield strength for a portion of lava tube L0.

the minimum yield strength, and this is valid also for τ_2. But the height of lava tube used does not consider the deposits of debris and sand that accumulated there, resulting in an underestimate of the height, which in fact is just a measurement of the present void, and then of τ_1.

- In the second model it was exploited the fact that Terrestrial overcrusted lava tube, as demonstrated by Kazumura cave, have asymmetry ratio close to 1, so it was considered a maximum depth equal to the measured width. It was also assumed that lava filled the tube, but this can happen only at the beginning of the emplacement because soon after the massive down-cutting of lava produced by thermal erosion creates a void space above the internal lava river. So the difference of the mean value of τ_2 from the other ones in table 5 can be a warning of wrong assumptions.

- In the third model it was assumed a circular section of the lava tube but the lava river did not fill the tube and a part of it solidified on the ground. So the measurement of τ_3 is supposed to be the minimum value of yield strength. The problem is that more than one lava flows could have occurred and so different lava layers could have overlapped taking away the possibility of estimating the thickness of one layer. In this third model the presence of debris in the lava tube were considered and estimated as bedrock from the collapsed roof. However, deposition of sand from eolian processes could occurred and collapses can form during the lava flow and the debris of the roof can be carried away leaving a flat bottom or other debris can be transported along the tube. Another problem of this model is that it was not possible to estimate the distance of the top of the roof from the above terrain, but, overall, it can be considered the most realistic between the other models.

A simplification that weakens the results of all the three models is surely the assumption of the behaviour of the lava during the emplacement as a Bingham fluid because lava is composed of three-phased material, so its dependence on viscosity is more complex than the assumed one and is also related to environmental conditions. Another source of uncertainty is related to the inclination of lava tubes because their longitudinal development can be not parallel to the ground, thus producing a proper slope that is not detectable from the surface. It was possible to estimate a deviation of the lava tube slope from the inclination of the ground by considering the mean depth of consequent skylights on the same identified lava tube. To perform the measurements of this deviation two long lava tubes collapsed in many points were considered. Since, as shown in figure 18, depths measured on CTX images are usually larger than those measured on HiRISE images, with almost a systematic error, it was measured the deviation of the slope for depths measured on CTX images, allowing to have results independent from the images used.
Figures 22 and 23 show the results for lava tube L0 and L9, respectively. On the top, the profile of the ground from MOLA data is plotted in blue, under which it is marked the distance of the bottom of the lava tube from the surface. Thus, it is visible the general trend of the longitudinal development of the two lava tubes respect to the ground. At the bottom of figures 22 and 23, the measured depths of the lava tubes along their paths are shown. Regarding lava tube L0, it can be observed that

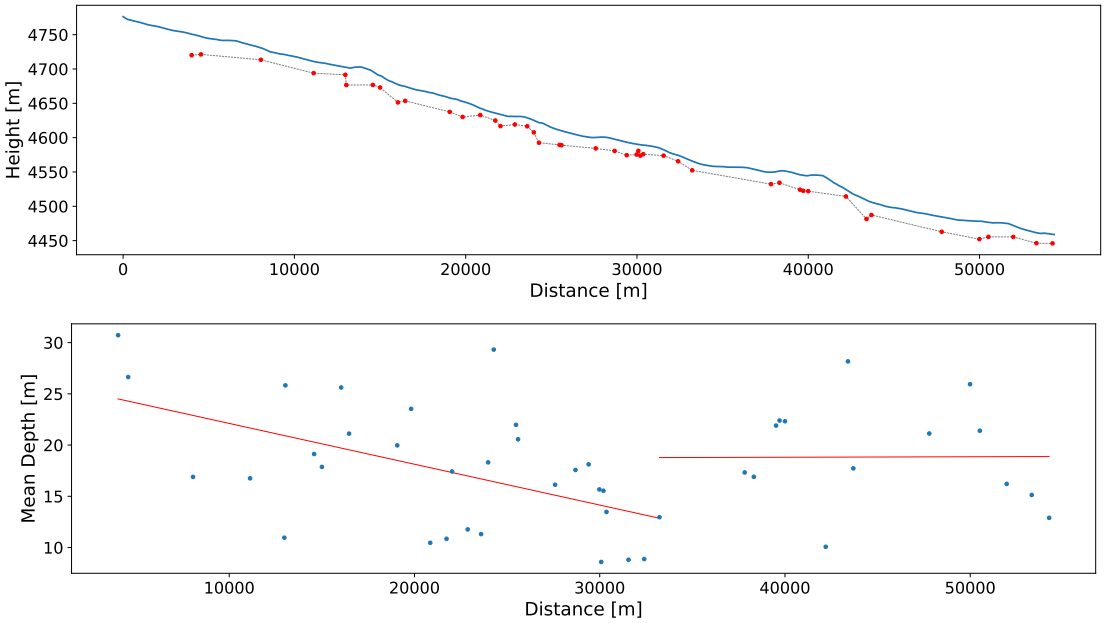

Figure 22: Top: Trend of the inclination of lava tube L0. Bottom: Depths measured along the track of lava tube L0. Two different deviations from the parallel to the ground were identified and fitted with two linear functions.

at the beginning it has a larger inclination than that of the ground, and afterwards it becomes parallel to it. This change in inclination was treated realising two linear fits. The first part of the lava tube, the most inclined, deviates from being parallel to the ground of $\sim 0.02°$, which is the 6% of 0.34°, the inclination of the ground (see tabel 7). The other fits give a deviation in degrees of the order of 10^{-4} and 10^{-3} for the last part of L0 and L9, respectively. It can be concluded that, considering the maximum measured deviation of 0.02°, the influence of the proper slope of the lava tubes on the final result of the yield strength can be neglected.

Despite all uncertainties contained in these methods for the evaluation of the yield strength, what was presented here are simple ways to estimate the rheological parameter τ and thus to better understand lava flows on Mars without direct measurements. Moreover, it can be assumed that the calculated values of yield strength can be considered as the conditions under which an empty cave can be left after a lava tube formation.

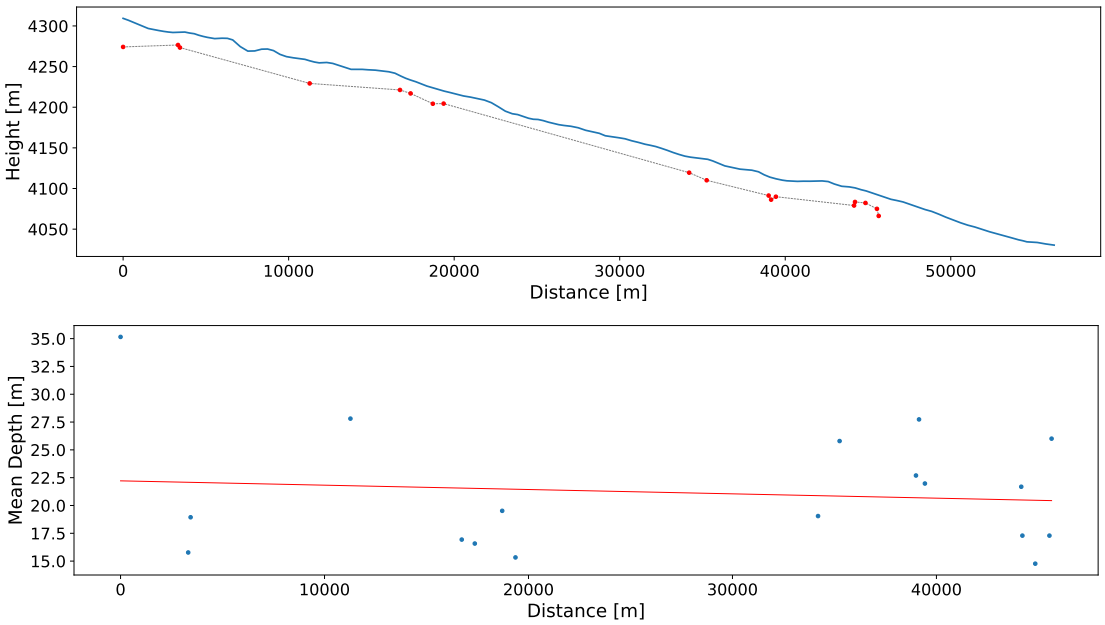

Figure 23: Top: Trend of the inclination of lava tube L9. Bottom: Depths measured along the track of lava tube L9. The inclination, which represents the deviation from the parallel to the ground was linearly fitted.

6 Future works and applications

The ultrafine resolution achieved by HiRISE is useful to determine morphological parameters of skylights and lava tubes, so it is important to provide this detailed accuracy for every feature discussed previously. It would be also useful observe the surface of Mars at larger emission and incidence angles, to have more insights on the cavities beneath the surface and also for studying the layer of bedrock exposed by the collapse, as described by Robinson et al. (2012) for the Moon.
To confirm the presence of an empty subsurface in correspondence of the discussed lava tubes or detect the presence of new lava tubes, which does not always display features on the surface, it would be helpful to analyse radar data from the SHARAD (SHAllow RADar) instrument of the Italian Space Agency, on board NASA's MRO. The characteristics of this instrument allow the study of the upper Km of the Martian surface and have great potential for detecting and characterising intact subsurface void spaces (Seu et al., 2004). The void is detected when the emitted radar wave encounters a dielectric contrast (e.g. free-space/ground): some of that energy is reflected back to the instrument ("returns") while the remaining energy continues to transmit through the subsurface, reflecting back to the instrument at deeper dielectric contrasts such as the interface between a basaltic layer and a cave interior (Perry et al., 2019). Kaku et al. (2017) nominally demonstrated this capability by reporting the detection of large caves in the Marius Hills region of the Moon using data from the Kaguya (SELENE) Lunar Radar Sounder (LRS) and these kind of studies are already ongoing on Mars, for example in the western flank of Alba Mons (Perry et al., 2019).

Exploration of lava tubes from the interior would give insights on the actual morphology of these structures, thus allowing to discover more about the history of Mars. Moreover, these caves are potential reservoirs of stable water-ice deposits, as discussed by Williams et al. (2010), where a small Martian cave was modelled to determine the stability and lifetime of an ice patch in the cave. It was shown that the cave air temperature remained at relatively stable level below the outside air temperature and favourable conditions for ice deposits were estimated in most of the Martian subsurface.
The exploration of Martian caves by robots requires particular technologies, such those developed by Kesner et al. (2007) and Kalita et al. (2018). In fact, the cave entrances have very deep vertical walls or steepen rim, the cave environment is wide and dark and the communication with the exterior difficult.
A problem with the actual technology is surely the landing on highly elevated region, such as Tharsis, due to the reduced atmospheric braking effect on entry probes, and the too much fuel required to active braking (Rossi and Van Gasselt, 2018).
The possibility of exploring lava tubes would be an important achievement for the astrobiological research because in caves there are stable conditions that preserve the environment from space weathering, dust winds and UV radiation, which make inhospitable the surface for life as we know it and delete possible traces of life (Léveillé and Datta, 2010). To better understand which biosignature can be found, microbiological researches in Terrestrial lava tubes were performed, in particular in the Corona lava tube system in which the presence of bacterial communities asso-

ciated with sulphates like gypsum and halite makes this cave an excellent analogue to what is expected to be found in the Martian subsurface in terms of geochemical environments and potential life forms (Sauro et al., 2019).
Projects on the astrobiological research in caves are currently being developed, such as NASA's Biologic and Resource Analog Investigations in Low Light Environments (BRAILLE), based on robotically executed astrobiology science and mapping activities in a lava cave (Blank, 2018), or the European Space Agency's PANGAEA training program, which is preparing astronauts to become effective partners of astrobiology scientists and mission engineers through exercises in analogue settings, including lava caves (Bessone et al., 2018).
For their insulating properties, lava tubes are particularly suitable and economical to host a human settlement, without the need of building shelters on the surface (Cushing, 2012).

7 Conclusions

In this work it was analysed an area at north of Arsia Mons, in which were considered 193 collapses of the ground that carried to the identification of 48 lava tubes, of which was estimated the average slope using MOLA data. A list of the newly identified lava tubes with their properties was created and for the first time measurements of the width of the considered presumable skylight-like apertures and estimates of the dimensions of the voids in the subsurface were performed. The estimate of the voids was performed exploiting the length of the rim shadow cast on the bottom of the collapsed lava tube. It was shown that the depths measured on CTX images have almost a systematic error that tend to overestimate the measurements, in comparison with the estimate performed with HiRISE images.
From the comparison between Martian and Terrestrial skylights of Kazumura cave, it was obtained that Martian skylights are larger, as expected, and emerged different values of asymmetry ratio. For Martian overcrusted lava tubes the asymmetry ratio displays elliptical sections, with value included between 0.295 and 0.465 and negligible quantifiable uncertainty, while Terrestrial lava tubes, from measurements of the internal structure, have a circular section with asymmetry ratio equals to 0.95 ± 0.04. Considering how the measurements were performed, the ellipticity of Martian lava tubes section can be an effect of the debris at the bottom of the skylights or ponding lava.
For this reason, different models of lava tubes were considered to perform the estimate of the yield strength, as the mean value of the average on each lava tube. For the model of lava tube with morphology displayed by measurements, the value of the yield strength is $\tau_1 = 1425.78 \pm 7.45$ Pa, the second model, of empty circular lava tube, gives a value of $\tau_2 = 742.62 \pm 2.78$ Pa and for the third model, of circular lava tube partially filled with debris and solidified lava, $\tau_3 = 1749.52 \pm 15.86$ Pa. These three values are in the range given by Hiesinger et al. (2015) ($2.54 \cdot 10^2$ Pa$< \tau < 9.63 \cdot 10^3$ Pa), that obtained these result with another method. It was also evaluated the possible proper inclination of lava tubes, that do not affect the result. The DTMs generated specifically for this work from stereo pair images of MRO's HiRISE and TGO's CaSSIS were used as comparison at higher reliability for the average slopes of lava tubes calculated with MOLA data that, despite the poor ground resolution, are reliable because they agree within their uncertainties. In fact, also the value of the yield strength measured using DTMs from MOLA and CaSSIS are compatible. DTMs were also employed to obtain the profile of a skylight section, which is rare to obtain due to usually bad conditions, and to perform an evaluation of the method used for estimating the depths of the collapses: measurements do not agree statistically and must be remind that the only quantifiable uncertainty of the measurements was given by the resolution of the images, excluding possible errors of inclination and emission angles, and also presumable errors performed by the operator, since measurements were executed manually.

8 Tables

Table 7: List of lava tubes considered in the region at North of Arsia Mons. Length in kilometres, coordinates of the centre and of the edges in degrees and number of skylights on each lava tube are listed.

Name	Length [km]	Sinuosity	Slope [deg]	Centre Latitude	Centre Longitude	Max. Latitude	Min. Latitude	Max. Longitude	Min. Longitude	Number of Skylights
L0	57.29	1.13	0.3	-3.22	-123.83	-2.84	-3.57	-124.05	-123.60	50
L1	5.56	1.05	0.4	-2.31	-125.48	-2.35	-2.27	-125.46	-125.50	2
L2	4.18	1.09	0.3	-2.66	-124.98	-2.67	-2.66	-124.95	-125.02	2
L3	56.24	1.14	0.4	-2.60	-125.02	-2.75	-2.39	-124.62	-125.37	15
L4	11.29	1.15	0.2	-2.88	-124.36	-2.95	-2.85	-124.30	-124.44	4
L5	6.82	1.05	0.4	-2.58	-124.92	-2.59	-2.56	-124.87	-124.97	1
L6	9.28	1.10	0.3	-2.84	-124.61	-2.90	-2.79	-124.57	-124.67	1
L7	29.88	1.13	0.4	-2.80	-123.15	-2.71	-2.87	-123.35	-122.94	7
L8	6.91	1.05	0.4	-2.36	-123.30	-2.38	-2.35	-123.36	-123.25	2
L9	56.23	1.12	0.3	-1.45	-123.94	-1.40	-1.42	-124.38	-123.53	18
L10	3.43	1.05	0.2	-1.33	-124.61	-1.32	-1.33	-124.63	-124.58	2
L11	19.04	1.07	0.4	-0.72	-125.08	-0.70	-0.74	-125.24	-124.94	2
L12	9.12	1.03	0.4	-0.64	-125.61	-0.61	-0.68	-125.68	-125.55	2
L13	7.46	1.10	0.2	-0.33	-125.09	-0.28	-0.34	-125.13	-125.03	1
L14	30.82	1.15	0.3	-0.25	-125.56	-0.12	-0.29	-125.74	-125.32	11
L15	2.77	1.06	0.3	-0.02	-125.68	-0.01	-0.04	-125.69	-125.66	5
L16	23.00	1.12	0.3	0.38	-125.91	0.37	0.39	-126.09	-125.74	0
L17	9.25	1.14	0.5	-0.05	-125.82	0.02	-0.10	-125.85	-125.79	12
L18	41.34	1.13	0.3	0.53	-125.90	0.63	0.52	-126.21	-125.60	8
L19	8.02	1.18	0.3	0.44	-125.50	0.45	0.46	-125.44	-125.55	1
L20	1.30	1.03	0.4	0.47	-125.35	0.47	0.47	-125.34	-125.36	2
L21	15.58	1.07	0.4	0.44	-125.18	0.41	0.50	-125.07	-125.30	5
L22	13.70	1.11	0.4	0.83	-125.90	0.88	0.82	-126.00	-125.80	3
L23	3.09	1.04	0.3	0.06	-125.64	0.06	0.06	-125.66	-125.61	2
L24	2.12	1.06	0.2	-0.04	-125.51	-0.03	-0.04	-125.53	-125.49	1
L25	2.04	1.02	0.3	0.05	-125.76	0.07	0.04	-125.77	-125.75	2
L26	3.57	1.04	0.5	-0.56	-125.82	-0.56	-0.56	-125.85	-125.79	1
L27	3.47	1.04	0.5	0.96	-124.08	0.95	0.97	-124.11	-124.06	1
L28	76.03	1.10	0.2	-0.45	-123.12	-0.33	-0.50	-122.57	-123.72	6
L29	2.53	1.11	0.7	0.87	-126.11	0.87	0.88	-126.13	-126.09	3
L30	5.91	1.05	0.4	-2.12	-125.73	-2.15	-2.08	-125.69	-125.76	2

Table 7: List of lava tubes considered in the region at North of Arsia Mons. Length in kilometres, coordinates of the centre and of the edges in degrees and number of skylights on each lava tube are listed.

Name	**Length [km]**	**Sinuosity**	**Slope [deg]**	**Centre Latitude**	**Centre Longitude**	**Max. Latitude**	**Min. Latitude**	**Max. Longitude**	**Min. Longitude**	**Number of Skylights**
L31	9.23	1.09	0.5	-2.65	-122.62	-2.70	-2.60	-122.56	-122.66	3
L32	6.17	1.07	0.4	-2.74	-122.47	-2.74	-2.71	-122.42	-122.51	1
L33	16.07	1.13	0.5	-2.85	-122.37	-2.93	-2.78	-122.29	-122.47	4
L34	19.16	1.03	0.8	-2.68	-121.50	-2.66	-2.70	-121.34	-121.65	3
L35	5.89	1.07	0.4	0.18	-126.02	0.19	0.17	-126.06	-125.97	3
L36	3.12	2.47	0.2	0.75	-126.17	0.73	0.73	-126.15	-126.15	1
L37	12.30	/	0.00	-3.02	-122.58	-3.03	-3.00	-122.68	-122.49	1
L38	60.94	/	0.01	1.00	-123.90	0.95	0.82	-123.44	-124.35	5
L39	14.56	1.29	0.6	-0.04	-126.62	-0.13	0.06	-126.54	-126.67	1
L40	11.47	0.21	1.4	0.33	-127.06	0.38	0.28	-127.13	-126.98	1
L41	17.92	1.36	0.3	1.09	-126.85	1.19	0.99	-126.93	-126.75	2
L42	10.58	1.00	0.4	-1.95	-126.06	-1.91	-2.01	-126.13	-126.01	3
L43	17.53	1.11	0.5	0.92	-123.05	0.84	0.86	-122.93	-123.16	1
L44	4.84	0.50	0.8	-0.09	-124.93	-0.06	-0.10	-124.96	-124.89	2
L45	4.99	0.37	0.6	0.45	-127.16	0.41	0.48	-127.14	-127.17	1
L46	40.26	8.67	0.02	0.68	-123.79	0.69	0.63	-123.77	-124.05	2
L47	80.83	/	0.03	0.39	-123.74	0.40	0.36	-123.75	-123.67	3

Table 8: List of skylights considered at North of Arsia Mons. Are presented coordinates, minimum depth measured exploiting the length of the shadow, width, length, asymmetry ratio (d/w), image on which measures were performed and lava tube on which they lie. Images whose name starts with "ESP" or "PSP" are from HiRISE, the others from CTX.

Name	**Longitude**	**Latitude**	**Min. Depth [m]**	**Width [m]**	**Length [m]**	**d/w**	**Image**	**Lava tube**
S1	-125.37	-2.39	16 ± 7	46	150	0.35 ± 0.16	D16_033474_1789_XN_01S125W	L3
S2	-125.36	-2.39	23 ± 7	56	146	0.42 ± 0.14	D16_033474_1789_XN_01S125W	L3
S3	-125.34	-2.41	7 ± 7	38	80	0.17 ± 0.19	D16_033474_1789_XN_01S125W	L3
S4	-125.19	-2.53	21 ± 7	57	118	0.37 ± 0.13	D16_033474_1789_XN_01S125W	L3
S5	-125.18	-2.54	17 ± 7	51	124	0.34 ± 0.15	D16_033474_1789_XN_01S125W	L3
S6	-125.18	-2.56	13 ± 7	52	80	0.25 ± 0.14	D16_033474_1789_XN_01S125W	L3
S7	-125.18	-2.56	17 ± 7	41	55	0.42 ± 0.18	D16_033474_1789_XN_01S125W	L3
S8	-125.05	-2.60	24 ± 8	56	122	0.42 ± 0.16	D12_031984_1786_XN_01S125W	L3
S9	-124.98	-2.62	29 ± 8	46	119	0.63 ± 0.20	D12_031984_1786_XN_01S125W	L3
S10	-124.68	-2.72	16 ± 8	43	74	0.38 ± 0.19	G12_022859_1787_XN_01S125W	L3
S11	-125.01	-2.66	17 ± 8	27	56	0.63 ± 0.34	D12_031984_1786_XN_01S125W	L2
S12	-124.43	-2.85	8.4 ± 0.3	34.3	37.0	0.24 ± 0.01	ESP_055337_1775	L4
S13	-124.41	-2.86	4.7 ± 0.3	15.0	24.0	0.31 ± 0.03	ESP_055337_1775	L4
S14	-124.04	-2.85	8.3 ± 0.4	17.7	25.6	0.47 ± 0.03	ESP_044419_1770	L0
S15	-124.03	-2.87	4.1 ± 0.4	22.8	29.9	0.18 ± 0.02	ESP_044419_1770	L0
S16	-124.03	-2.89	7.8 ± 0.4	49.1	78.9	0.16 ± 0.01	ESP_044419_1770	L0
S17	-124.03	-2.91	12.8 ± 0.4	38.3	42.5	0.33 ± 0.01	ESP_044419_1770	L0
S18	-124.02	-2.92	17.1 ± 0.4	51.2	90.2	0.33 ± 0.01	ESP_044419_1770	L0
S19	-123.99	-2.94	13.9 ± 0.4	29.1	33.8	0.48 ± 0.02	ESP_044419_1770	L0
S20	-123.96	-3.00	10.9 ± 0.3	41.2	56.0	0.26 ± 0.01	ESP_037232_1770	L0
S21	-123.96	-3.00	13.9 ± 0.8	55.1	117.7	0.25 ± 0.01	ESP_037232_1770	L0
S22	-123.94	-3.01	10.8 ± 0.8	53.8	118.7	0.20 ± 0.01	ESP_037232_1770	L0
S23	-123.93	-3.04	16.5 ± 0.3	39.2	56.2	0.42 ± 0.01	ESP_037232_1770	L0
S24	-123.93	-3.05	12.8 ± 0.3	34.4	69.6	0.37 ± 0.01	ESP_037232_1770	L0
S25	-123.93	-3.05	15.5 ± 0.3	32.0	58.2	0.48 ± 0.02	ESP_037232_1770	L0
S26	-123.93	-3.07	8.8 ± 0.3	34.5	57.9	0.25 ± 0.01	ESP_037232_1770	L0
S27	-123.92	-3.08	11.5 ± 0.5	45.2	48.9	0.25 ± 0.01	ESP_037232_1770	L0
S28	-123.89	-3.15	12.0 ± 0.5	42.9	51.5	0.28 ± 0.01	ESP_037232_1770	L0
S29	-123.88	-3.16	9 ± 4	28	29	0.32 ± 0.17	F22_044419_1771_XN_02S124W	L0
S30	-123.87	-3.17	9 ± 4	28	43	0.32 ± 0.17	F22_044419_1771_XN_02S124W	L0

Table 8: List of skylights considered at North of Arsia Mons. Are presented coordinates, minimum depth measured exploiting the length of the shadow, width, length, asymmetry ratio (d/w), image on which measures were performed and lava tube on which they lie. Images whose name starts with "ESP" or "PSP" are from HiRISE, the others from CTX.

Name	**Longitude**	**Latitude**	**Min. Depth [m]**	**Width [m]**	**Length [m]**	**d/w**	**Image**	**Lava tube**
S31	-123.86	-3.18	13 ± 4	50	68	0.27 ± 0.09	F22_044419_1771_XN_02S124W	L0
S32	-123.86	-3.19	16 ± 4	48	75	0.32 ± 0.10	F22_044419_1771_XN_02S124W	L0
S33	-123.85	-3.19	9 ± 4	32	49	0.27 ± 0.14	F22_044419_1771_XN_02S124W	L0
S34	-123.85	-3.19	16 ± 4	40	76	0.39 ± 0.12	F22_044419_1771_XN_02S124W	L0
S35	-123.85	-3.20	18 ± 4	42	72	0.43 ± 0.12	F22_044419_1771_XN_02S124W	L0
S36	-123.84	-3.21	18 ± 4	52	82	0.34 ± 0.09	F22_044419_1771_XN_02S124W	L0
S37	-123.83	-3.22	16 ± 4	48	79	0.33 ± 0.10	F22_044419_1771_XN_02S124W	L0
S38	-123.80	-3.24	21 ± 4	65	83	0.32 ± 0.07	F22_044419_1771_XN_02S124W	L0
S39	-123.80	-3.24	22 ± 4	78	86	0.28 ± 0.06	F22_044419_1771_XN_02S124W	L0
S40	-123.80	-3.26	29 ± 4	49	89	0.59 ± 0.11	F22_044419_1771_XN_02S124W	L0
S41	-123.80	-3.27	18 ± 4	69	112	0.27 ± 0.07	F22_044419_1771_XN_02S124W	L0
S42	-123.80	-3.27	11 ± 4	32	52	0.35 ± 0.14	P20_008763_1749_XN_05S123W	L0
S43	-123.79	-3.28	12 ± 4	26	33	0.45 ± 0.18	P20_008763_1749_XN_05S123W	L0
S44	-123.77	-3.28	17 ± 4	59	84	0.30 ± 0.07	P20_008763_1749_XN_05S123W	L0
S45	-123.77	-3.28	11 ± 4	32	39	0.34 ± 0.14	P20_008763_1749_XN_05S123W	L0
S46	-123.76	-3.30	10 ± 4	32	49	0.33 ± 0.14	P20_008763_1749_XN_05S123W	L0
S47	-123.75	-3.31	24 ± 4	60	92	0.39 ± 0.08	P20_008763_1749_XN_05S123W	L0
S48	-123.74	-3.31	20 ± 4	65	90	0.31 ± 0.07	P20_008763_1749_XN_05S123W	L0
S49	-123.72	-3.35	21 ± 4	61	70	0.34 ± 0.07	P20_008763_1749_XN_05S123W	L0
S50	-123.72	-3.35	17.3 ± 0.5	70.2	98.1	0.25 ± 0.01	ESP_017901_1765	L0
S51	-123.72	-3.37	8.9 ± 0.3	41.5	45.1	0.21 ± 0.01	ESP_017901_1765	L0
S52	-123.71	-3.38	10.1 ± 0.5	34.8	42.0	0.29 ± 0.02	ESP_017901_1765	L0
S53	-123.70	-3.40	11.3 ± 0.5	48.0	64.6	0.24 ± 0.01	ESP_017901_1765	L0
S54	-123.70	-3.40	7.2 ± 0.7	22.5	27.9	0.32 ± 0.03	ESP_017901_1765	L0
S55	-123.70	-3.43	6.7 ± 0.3	33.2	46.5	0.20 ± 0.01	ESP_017901_1765	L0
S56	-123.68	-3.47	7.1 ± 0.3	30.8	41.2	0.23 ± 0.01	ESP_017901_1765	L0
S57	-123.63	-3.51	27 ± 4	49	81	0.54 ± 0.11	B21_017901_1787_XN_01S124W	L0
S58	-123.63	-3.52	31 ± 4	58	91	0.53 ± 0.09	B21_017901_1787_XN_01S124W	L0
S59	-125.23	-2.50	52 ± 7	53	86	0.98 ± 0.17	D16_033474_1789_XN_01S125W	L3
S60	-125.23	-2.50	13 ± 7	27	35	0.47 ± 0.29	D16_033474_1789_XN_01S125W	L3

Table 8: List of skylights considered at North of Arsia Mons. Are presented coordinates, minimum depth measured exploiting the length of the shadow, width, length, asymmetry ratio (d/w), image on which measures were performed and lava tube on which they lie. Images whose name starts with "ESP" or "PSP" are from HiRISE, the others from CTX.

Name	**Longitude**	**Latitude**	**Min. Depth [m]**	**Width [m]**	**Length [m]**	**d/w**	**Image**	**Lava tube**
S61	-125.48	-2.32	24 ± 4	59	96	0.41 ± 0.08	G03_019457_1777_XN_02S125W	L1
S62	-125.48	-2.32	19 ± 4	33	48	0.57 ± 0.17	G03_019457_1777_XN_02S125W	L1
S63	-124.97	-2.63	27 ± 8	44	61	0.61 ± 0.20	G12_022859_1787_XN_01S125W	L3
S64	-125.85	0.17	20 ± 7	36	50	0.55 ± 0.22	G16_024626_1795_XN_00S125W	/
S65	-125.54	0.01	22 ± 7	64	79	0.34 ± 0.12	D16_033474_1789_XN_01S125W	/
S66	-125.90	0.07	22 ± 4	64	89	0.35 ± 0.08	G23_027382_1803_XN_00N126W	/
S67	-126.15	0.73	17 ± 4	37	50	0.47 ± 0.14	G23_027382_1803_XN_00N126W	L36
S68	-122.64	-3.02	17 ± 4	38	61	0.46 ± 0.12	B01_010187_1759_XI_04S122W	L37
S69	-121.35	-2.67	21 ± 5	39	71	0.53 ± 0.15	B18_016490_1749_XN_05S121W	L34
S70	-126.11	0.87	19 ± 4	37	73	0.52 ± 0.14	G23_027382_1803_XN_00N126W	L29
S71	-126.11	0.87	18 ± 4	37	67	0.50 ± 0.14	G23_027382_1803_XN_00N126W	L29
S72	-125.99	0.88	16 ± 4	38	58	0.43 ± 0.14	G23_027382_1803_XN_00N126W	L22
S73	-125.98	0.88	17 ± 4	36	54	0.48 ± 0.15	G23_027382_1803_XN_00N126W	L22
S74	-125.96	0.87	24 ± 7	40	52	0.61 ± 0.21	G16_024626_1795_XN_00S125W	L22
S75	-125.76	0.54	29 ± 7	57	67	0.51 ± 0.14	G16_024626_1795_XN_00S125W	L18
S76	-125.76	0.54	25 ± 7	36	49	0.70 ± 0.24	G16_024626_1795_XN_00S125W	L18
S77	-125.73	0.54	24 ± 7	48	73	0.51 ± 0.17	G16_024626_1795_XN_00S125W	L18
S78	-125.73	0.53	27 ± 7	48	75	0.57 ± 0.17	G16_024626_1795_XN_00S125W	L18
S79	-126.05	0.19	17 ± 4	24	27	0.72 ± 0.26	G23_027382_1803_XN_00N126W	L35
S80	-126.05	0.19	23 ± 4	60	113	0.38 ± 0.08	G23_027382_1803_XN_00N126W	L35
S81	-125.84	0.01	39 ± 7	55	120	0.71 ± 0.16	G16_024626_1795_XN_00S125W	L17
S82	-125.84	0.01	25 ± 7	40	57	0.62 ± 0.21	G16_024626_1795_XN_00S125W	L17
S83	-125.83	0.00	20 ± 7	31	36	0.63 ± 0.27	G16_024626_1795_XN_00S125W	L17
S84	-125.82	-0.04	40 ± 7	57	80	0.70 ± 0.15	G16_024626_1795_XN_00S125W	L17
S85	-125.82	-0.04	27 ± 7	45	72	0.59 ± 0.18	G16_024626_1795_XN_00S125W	L17
S86	-125.82	-0.05	21 ± 7	38	39	0.56 ± 0.22	G16_024626_1795_XN_00S125W	L17
S87	-125.81	-0.09	36 ± 7	60	139	0.59 ± 0.14	G16_024626_1795_XN_00S125W	L17
S88	-125.80	-0.09	24 ± 7	41	53	0.59 ± 0.20	G16_024626_1795_XN_00S125W	L17
S89	-125.80	-0.10	28 ± 7	39	47	0.71 ± 0.22	G16_024626_1795_XN_00S125W	L17
S90	-125.79	-0.10	53 ± 7	37	58	1.44 ± 0.31	G16_024626_1795_XN_00S125W	L17

Table 8: List of skylights considered at North of Arsia Mons. Are presented coordinates, minimum depth measured exploiting the length of the shadow, width, length, asymmetry ratio (d/w), image on which measures were performed and lava tube on which they lie. Images whose name starts with "ESP" or "PSP" are from HiRISE, the others from CTX.

Name	**Longitude**	**Latitude**	**Min. Depth [m]**	**Width [m]**	**Length [m]**	**d/w**	**Image**	**Lava tube**
S91	-125.79	-0.10	21 ± 7	50	67	0.42 ± 0.16	G16_024626_1795_XN_00S125W	L17
S92	-125.73	-0.12	23 ± 7	34	57	0.66 ± 0.25	G16_024626_1795_XN_00S125W	L14
S93	-125.68	-0.13	18 ± 7	40	50	0.45 ± 0.20	G16_024626_1795_XN_00S125W	L14
S94	-125.68	-0.14	14 ± 7	29	33	0.50 ± 0.28	G16_024626_1795_XN_00S125W	L14
S95	-125.68	-0.15	20 ± 7	36	47	0.57 ± 0.23	G16_024626_1795_XN_00S125W	L14
S96	-125.68	-0.15	25 ± 7	60	83	0.41 ± 0.13	G16_024626_1795_XN_00S125W	L14
S97	-125.63	-0.20	28 ± 7	47	71	0.59 ± 0.17	G16_024626_1795_XN_00S125W	L14
S98	-125.49	-0.28	26 ± 7	48	70	0.54 ± 0.16	D16_033474_1789_XN_01S125W	L14
S99	-125.41	-0.28	27 ± 7	36	66	0.73 ± 0.23	D16_033474_1789_XN_01S125W	L14
S100	-125.80	-0.56	24 ± 7	44	58	0.54 ± 0.18	G16_024626_1795_XN_00S125W	L26
S101	-125.67	-0.62	20 ± 7	38	53	0.52 ± 0.21	G16_024626_1795_XN_00S125W	L12
S102	-125.73	-2.11	22 ± 4	46	72	0.48 ± 0.12	G23_027382_1803_XN_00N126W	L30
S103	-125.71	-2.13	22 ± 4	48	87	0.47 ± 0.11	G23_027382_1803_XN_00N126W	L30
S104	-125.53	0.44	24 ± 7	43	156	0.56 ± 0.19	D16_033474_1789_XN_01S125W	L19
S105	-125.35	0.47	32 ± 8	38	42	0.84 ± 0.25	G12_022859_1787_XN_01S125W	L20
S106	-125.29	0.50	32 ± 8	39	66	0.82 ± 0.24	G12_022859_1787_XN_01S125W	L21
S107	-125.27	0.49	23 ± 8	24	31	0.99 ± 0.43	G12_022859_1787_XN_01S125W	L21
S108	-125.27	0.49	24 ± 8	47	65	0.51 ± 0.18	G12_022859_1787_XN_01S125W	L21
S109	-125.10	0.42	28 ± 8	47	114	0.60 ± 0.19	G12_022859_1787_XN_01S125W	L21
S110	-125.10	0.42	40 ± 8	56	79	0.71 ± 0.16	G12_022859_1787_XN_01S125W	L21
S111	-124.94	-0.07	26 ± 8	51	109	0.51 ± 0.17	G12_022859_1787_XN_01S125W	L44
S112	-124.95	-0.07	15 ± 8	31	41	0.49 ± 0.27	G12_022859_1787_XN_01S125W	L44
S113	-125.10	-0.31	29 ± 8	58	87	0.51 ± 0.15	G12_022859_1787_XN_01S125W	L13
S114	-125.23	-0.70	25 ± 8	48	82	0.52 ± 0.19	D12_031984_1786_XN_01S125W	L11
S115	-125.18	-0.71	23 ± 8	38	76	0.61 ± 0.24	D12_031984_1786_XN_01S125W	L11
S116	-124.62	-1.33	24 ± 9	52	96	0.46 ± 0.17	D15_032907_1789_XN_01S124W	L10
S117	-124.60	-1.33	27 ± 9	49	80	0.55 ± 0.19	D15_032907_1789_XN_01S124W	L10
S118	-124.22	-1.43	26 ± 4	45	91	0.58 ± 0.12	G20_025905_1784_XN_01S124W	L9
S119	-124.22	-1.43	17 ± 4	31	48	0.56 ± 0.18	G20_025905_1784_XN_01S124W	L9
S120	-124.21	-1.43	15 ± 4	31	49	0.48 ± 0.17	G20_025905_1784_XN_01S124W	L9

Table 8: List of skylights considered at North of Arsia Mons. Are presented coordinates, minimum depth measured exploiting the length of the shadow, width, length, asymmetry ratio (d/w), image on which measures were performed and lava tube on which they lie. Images whose name starts with "ESP" or "PSP" are from HiRISE, the others from CTX.

Name	**Longitude**	**Latitude**	**Min. Depth [m]**	**Width [m]**	**Length [m]**	**d/w**	**Image**	**Lava tube**
S121	-124.20	-1.44	17 ± 4	35	48	0.50 ± 0.15	G20_025905_1784_XN_01S124W	L9
S122	-124.20	-1.44	22 ± 4	39	62	0.56 ± 0.14	G20_025905_1784_XN_01S124W	L9
S123	-124.13	-1.45	22 ± 4	44	85	0.50 ± 0.12	G20_025905_1784_XN_01S124W	L9
S124	-124.12	-1.45	28 ± 4	48	81	0.58 ± 0.12	G20_025905_1784_XN_01S124W	L9
S125	-124.12	-1.45	23 ± 4	46	118	0.50 ± 0.11	G20_025905_1784_XN_01S124W	L9
S126	-124.06	-1.46	26 ± 4	48	95	0.54 ± 0.11	G20_025905_1784_XN_01S124W	L9
S127	-124.04	-1.46	19 ± 4	46	94	0.42 ± 0.11	B21_017901_1787_XN_01S124W	L9
S128	-123.80	-1.48	15 ± 5	56	152	0.27 ± 0.10	J22_053280_1791_XI_00S123W	L9
S129	-123.79	-1.47	20 ± 5	45	81	0.43 ± 0.13	J22_053280_1791_XI_00S123W	L9
S130	-123.77	-1.48	17 ± 5	33	47	0.51 ± 0.19	J22_053280_1791_XI_00S123W	L9
S131	-123.76	-1.48	17 ± 5	49	104	0.34 ± 0.12	J22_053280_1791_XI_00S123W	L9
S132	-123.57	-1.39	7.3 ± 0.6	55.4	57.3	0.13 ± 0.01	ESP_016767_1785	L9
S133	-123.57	-1.39	5.9 ± 0.6	23.9	30.3	0.25 ± 0.03	ESP_016767_1785	L9
S134	-123.53	-1.42	12.7 ± 0.8	46.0	77.1	0.28 ± 0.02	ESP_016767_1785	L9
S135	-123.96	0.98	29 ± 5	64	164	0.46 ± 0.09	J22_053280_1791_XI_00S123W	L38
S136	-123.96	0.98	27 ± 5	52	100	0.51 ± 0.12	J22_053280_1791_XI_00S123W	L38
S137	-123.42	-0.45	23 ± 4	30	61	0.78 ± 0.21	D02_028160_1794_XN_00S123W	L28
S138	-123.23	-0.47	18 ± 5	39	55	0.47 ± 0.14	G21_026472_1801_XN_00N123W	L28
S139	-123.18	-0.46	17 ± 5	50	77	0.35 ± 0.10	G21_026472_1801_XN_00N123W	L28
S140	-123.10	-0.45	24 ± 5	62	158	0.38 ± 0.08	G21_026472_1801_XN_00N123W	L28
S141	-123.08	-0.45	26 ± 5	49	70	0.54 ± 0.11	G21_026472_1801_XN_00N123W	L28
S142	-123.31	-2.36	19 ± 4	48	76	0.41 ± 0.10	D02_028160_1794_XN_00S123W	L8
S143	-123.26	-2.35	28 ± 4	61	75	0.46 ± 0.08	D02_028160_1794_XN_00S123W	L8
S144	-123.34	-2.72	28 ± 5	56	141	0.51 ± 0.11	J22_053280_1791_XI_00S123W	L7
S145	-123.30	-2.77	33 ± 5	51	91	0.66 ± 0.13	J22_053280_1791_XI_00S123W	L7
S146	-123.08	-2.82	22 ± 5	49	66	0.45 ± 0.11	F21_043997_1753_XI_04S122W	L7
S147	-123.04	-2.83	21 ± 5	55	74	0.39 ± 0.10	F21_043997_1753_XI_04S122W	L7
S148	-122.66	-2.61	23 ± 4	58	65	0.40 ± 0.09	B20_017479_1792_XN_00S122W	L31
S149	-122.63	-2.65	23 ± 4	53	83	0.43 ± 0.10	B20_017479_1792_XN_00S122W	L31
S150	-122.59	-2.68	27 ± 4	51	99	0.53 ± 0.11	B20_017479_1792_XN_00S122W	L31

Table 8: List of skylights considered at North of Arsia Mons. Are presented coordinates, minimum depth measured exploiting the length of the shadow, width, length, asymmetry ratio (d/w), image on which measures were performed and lava tube on which they lie. Images whose name starts with "ESP" or "PSP" are from HiRISE, the others from CTX.

Name	**Longitude**	**Latitude**	**Min. Depth [m]**	**Width [m]**	**Length [m]**	**d/w**	**Image**	**Lava tube**
S151	-122.42	-2.74	9 ± 4	39	40	0.23 ± 0.12	B20_017479_1792_XN_00S122W	L32
S152	-122.44	-2.78	36 ± 4	61	119	0.59 ± 0.09	B20_017479_1792_XN_00S122W	L33
S153	-122.43	-2.78	27 ± 4	47	80	0.57 ± 0.12	B20_017479_1792_XN_00S122W	L33
S154	-122.42	-2.79	30 ± 4	53	90	0.56 ± 0.11	B20_017479_1792_XN_00S122W	L33
S155	-122.34	-2.87	23 ± 4	43	70	0.53 ± 0.13	B20_017479_1792_XN_00S122W	L33
S156	-125.77	0.07	25 ± 7	58	117	0.43 ± 0.14	G16_024626_1795_XN_00S125W	L25
S157	-125.76	0.06	20 ± 7	48	59	0.43 ± 0.17	G16_024626_1795_XN_00S125W	L25
S158	-125.65	0.07	19 ± 7	34	73	0.55 ± 0.23	D16_033474_1789_XN_01S125W	L23
S159	-125.65	0.07	19 ± 7	28	33	0.69 ± 0.30	D16_033474_1789_XN_01S125W	L23
S160	-125.68	-0.02	22 ± 7	40	70	0.55 ± 0.20	D16_033474_1789_XN_01S125W	L15
S161	-125.68	-0.02	29 ± 7	52	66	0.56 ± 0.15	D16_033474_1789_XN_01S125W	L15
S162	-125.67	-0.03	29 ± 7	55	88	0.52 ± 0.14	D16_033474_1789_XN_01S125W	L15
S163	-125.66	-0.04	19 ± 7	43	77	0.45 ± 0.18	D16_033474_1789_XN_01S125W	L15
S164	-125.67	-0.03	29 ± 7	57	138	0.51 ± 0.14	D16_033474_1789_XN_01S125W	L15
S165	-126.66	0.03	19 ± 5	43	48	0.45 ± 0.13	J05_046740_1802_XN_00N126W	L39
S166	-127.10	0.37	13.7 ± 1.0	39.1	128.5	0.35 ± 0.03	ESP_049021_1805	L40
S167	-127.16	0.46	20 ± 4	41	99	0.49 ± 0.13	D02_027870_1803_XN_00N127W	L45
S168	-126.12	0.58	22 ± 4	46	93	0.48 ± 0.11	G23_027382_1803_XN_00N126W	L18
S169	-126.21	0.62	29 ± 8	44	76	0.66 ± 0.21	D14_032762_1810_XN_01N126W	L18
S170	-126.28	0.89	37 ± 8	39	56	0.94 ± 0.26	D14_032762_1810_XN_01N126W	/
S171	-126.79	1.04	19 ± 5	37	60	0.50 ± 0.15	J05_046740_1802_XN_00N126W	L41
S172	-126.08	-1.95	18 ± 6	42	82	0.44 ± 0.16	G10_022147_1782_XN_01S126W	L42
S173	-126.08	-1.95	19 ± 6	46	62	0.43 ± 0.14	G10_022147_1782_XN_01S126W	L42
S174	-126.10	-1.94	19 ± 6	43	64	0.45 ± 0.15	G10_022147_1782_XN_01S126W	L42
S175	-123.08	0.91	18 ± 4	46	60	0.39 ± 0.11	B20_017479_1792_XN_00S122W	L43
S176	-123.70	-1.42	18.2 ± 0.9	53.4	83.1	0.34 ± 0.02	ESP_016556_1785	L9
S177	-122.73	-0.31	18 ± 4	44	62	0.42 ± 0.12	B20_017479_1792_XN_00S122W	/
S178	-124.97	-2.56	18 ± 8	36	44	0.48 ± 0.24	D12_031984_1786_XN_01S125W	L5
S179	-124.00	-2.86	6.7 ± 0.4	19.3	25.2	0.35 ± 0.03	ESP_044419_1770	/
S180	-124.65	-2.80	17 ± 8	45	84	0.39 ± 0.19	G12_022859_1787_XN_01S125W	L6

Table 8: List of skylights considered at North of Arsia Mons. Are presented coordinates, minimum depth measured exploiting the length of the shadow, width, length, asymmetry ratio (d/w), image on which measures were performed and lava tube on which they lie. Images whose name starts with "ESP" or "PSP" are from HiRISE, the others from CTX.

Name	**Longitude**	**Latitude**	**Min. Depth [m]**	**Width [m]**	**Length [m]**	**d/w**	**Image**	**Lava tube**
S181	-125.59	-0.66	21 ± 7	41	49	0.50 ± 0.19	G16_024626_1795_XN_00S125W	L12
S182	-125.52	-0.04	21 ± 7	27	56	0.77 ± 0.31	D16_033474_1789_XN_01S125W	L24
S183	-124.11	0.95	18 ± 5	62	85	0.28 ± 0.09	J22_053280_1791_XI_00S123W	L27
S184	-124.32	0.83	14 ± 4	43	58	0.32 ± 0.11	B21_017901_1787_XN_01S124W	L38
S185	-124.03	0.95	20 ± 5	50	82	0.39 ± 0.12	J22_053280_1791_XI_00S123W	L38
S186	-123.99	0.97	16 ± 5	74	144	0.22 ± 0.07	J22_053280_1791_XI_00S123W	L38
S187	-123.66	0.57	11.6 ± 0.4	62.7	91.1	0.19 ± 0.01	ESP_028160_1805	L46
S188	-123.67	0.59	24.0 ± 0.4	46.0	48.0	0.52 ± 0.01	ESP_028160_1805	L46
S189	-123.85	0.43	28 ± 5	52	91	0.53 ± 0.12	J22_053280_1791_XI_00S123W	L47
S190	-123.75	0.40	24 ± 4	43	71	0.56 ± 0.13	D02_028160_1794_XN_00S123W	L47
S191	-123.75	0.40	19 ± 4	47	71	0.41 ± 0.11	D02_028160_1794_XN_00S123W	L47
S192	-121.63	-2.70	14 ± 4	37	61	0.38 ± 0.13	K05_055482_1771_XN_02S121W	L34
S193	-121.65	-2.70	18 ± 4	33	63	0.54 ± 0.16	K05_055482_1771_XN_02S121W	L34

Table 9: List of skylights around Arsia Mons.

Longitude	**Latitude**	**Min. Depth [m]**	**Width [m]**	**d/w**	**Image**
-119.54	-0.95	15.8 ± 0.3	25.4	0.62 ± 0.03	ESP_057434_1790
-120.07	-11.57	14.2 ± 0.1	31.3	0.45 ± 0.02	ESP_044287_1685
-118.70	-1.69	28.4 ± 0.6	41.5	0.68 ± 0.02	ESP_058489_1785
-116.76	-4.50	34	45	0.76	B01_009989_1758
-123.66	-13.89	75	50	1.50	P13_005968_1674
-116.25	-6.18	35	50	0.70	G11_022384_1742
-116.97	-4.21	35.0	55	0.64	PSP_009989_1760
-123.24	-13.86	85	60	1.42	P12_005757_1637
-119.47	-1.05	51	60	0.85	G16_024428_1763
-117.92	-2.86	23.2 ± 0.5	54.6	0.43 ± 0.01	ESP_058133_1770
-117.37	-5.29	57.0	60	0.95	PSP_007774_1745
-102.88	12.64	44	60	0.73	P11_005321_1913
-124.82	0.88	40.7 ± 0.4	67.0	0.61 ± 0.01	ESP_058687_1810
-118.70	-12.40	42	65	0.65	P15_006838_1657
-117.76	-2.72	34.5 ± 0.3	65.6	0.53 ± 0.01	ESP_057645_1770
-119.54	-0.95	47.7 ± 0.3	67.4	0.71 ± 0.01	ESP_057434_1790
-119.28	1.05	32.7 ± 0.4	91.1	0.36 ± 0.01	ESP_051803_1810
-121.19	-19.40	36.6 ± 0.2	95.2	0.38 ± 0.01	ESP_055614_1605
-117.81	-2.65	41	90	0.46	P17_007774_1757
-122.47	-14.53	52	100	0.52	P12_005546_1642
-118.75	-13.54	45.3 ± 0.5	119.9	0.38 ± 0.01	ESP_056946_1665
-120.36	-1.67	82.0	115	0.71	ESP_013786_1785
-120.10	-11.35	66	110	0.60	P10_005124_1708
-121.69	-14.36	44	115	0.38	P11_005335_1668
-119.09	-7.16	129.0	120	1.08	ESP_028450_1730
-123.49	-13.96	39	125	0.31	P19_008328_1638
-122.51	-14.00	44	125	0.35	G18_025338_1674
-120.05	-13.92	76	120	0.63	P14_006548_1653
-121.23	-14.06	45	130	0.35	P18_008117_1647
-120.21	-14.85	47	130	0.36	B17_016134_1651
-124.59	-14.21	54	140	0.39	G18_025404_1661
-119.98	-13.84	65.0 ± 0.3	125.0	0.52 ± 0.01	ESP_033342_1660

Table 9: List of skylights around Arsia Mons.

Longitude	**Latitude**	**Min. Depth [m]**	**Width [m]**	**d/w**	**Image**
-122.44	-14.51	65.8 ± 0.2	170.0	0.39 ± 0.01	ESP_028793_1655
-119.96	-14.28	59.0 ± 0.2	160.0	0.37 ± 0.01	ESP_012600_1655
-123.38	-12.60	63	180	0.35	P17_007827_1697
-121.88	-18.90	112	185	0.61	P14_006614_1597
-112.45	17.28	80.0	200	0.40	PSP_003317_1975
-122.61	-19.58	60	215	0.28	B17_016411_1594
-121.59	-18.55	69.0	240	0.29	ESP_030995_1610
-119.97	-6.52	155.0	250	0.62	ESP_011756_1735
-112.46	17.27	167.0	275	0.61	PSP_003317_1975
-122.44	-19.46	124.0	475	0.26	ESP_016411_1605
-119.05	-0.55	45.0	105.0	0.43	PSP_010055_1795
-117.47	-17.46	151.0	195.0	0.77	ESP_021738_1625
-124.06	-18.65	73	85	0.86	B08_012587_1616
-123.47	-13.09	46	190	0.24	B22_018112_1667
-120.01	-11.58	10.8	36.8	0.29	ESP_044287_1685
-120.34	-11.52	18.5	50.3	0.37	ESP_043153_1685
-123.93	-13.95	46.68 ± 0.55	191.4	0.24 ± 0.01	ESP_058186_1660

References

Albee, A. L., R. E. Arvidson, F. Palluconi, and T. Thorpe
2001. Overview of the Mars Global Surveyor mission. *Journal of Geophysical Research: Planets*, 106(E10):23291–23316.

Allred, K. and C. Allred
2002. Kazumura Cave Atlas, Island of Hawai'i. *Hawaii Speleological Survey*.

Allred, K. L. and C. Allred
1997. Development and morphology of Kazumura cave, Hawaii.

Atwood-Stone, C. and A. S. McEwen
2013. Avalanche slope angles in low-gravity environments from active Martian sand dunes. *Geophysical Research Letters*, 40(12):2929–2934.

Bandfield, J. L., C. S. Edwards, D. R. Montgomery, and B. D. Brand
2013. The dual nature of the martian crust: Young lavas and old clastic materials. *Icarus*, 222(1):188 – 199.

Bandfield, J. L., V. E. Hamilton, and P. R. Christensen
2000. A Global View of Martian Surface Compositions from MGS-TES. *Science*, 287(5458):1626–1630.

Bessone, L., F. Sauro, M. Maurer, and M. Piens
2018. Testing technologies and operational concepts for field geology exploration of the Moon and beyond: the ESA PANGAEA-X campaign. In *EGU General Assembly Conference Abstracts*, volume 20, P. 4013.

Beyer, R. A., O. Alexandrov, and S. McMichael
2018. The Ames Stereo Pipeline: NASA's Open Source Software for Deriving and Processing Terrain Data. *Earth and Space Science*, 5(9):537–548.

Blair, D. M., L. Chappaz, R. Sood, C. Milbury, A. Bobet, H. J. Melosh, K. C. Howell, and A. M. Freed
2017. The structural stability of lunar lava tubes. *Icarus*, 282:47 – 55.

Blank, J.
2018. Preparing for Robotic Astrobiology Missions to Lava Caves on Mars: The BRAILLE Project at Lava Beds National Monument (N. CA, USA). In *42nd COSPAR Scientific Assembly*, volume 42, Pp. F3.1–13–18.

Bleacher, J. E., R. Greeley, D. A. Williams, S. R. Cave, and G. Neukum
2007a. Trends in effusive style at the Tharsis Montes, Mars, and implications for the development of the Tharsis province. *Journal of Geophysical Research: Planets*, 112(E9).

Bleacher, J. E., R. Greeley, D. A. Williams, S. C. Werner, E. Hauber, and G. Neukum
2007b. Olympus Mons, Mars: Inferred changes in late Amazonian aged effusive activity from lava flow mapping of Mars Express High Resolution Stereo Camera data. *Journal of Geophysical Research: Planets*, 112(E4).

Carr, M. H.
2007. *The Surface of Mars*, Cambridge Planetary Science. Cambridge University Press.

Cushing, G. E.
2012. Candidate cave entrances on Mars. *Journal of Cave and Karst Studies*.

Cushing, G. E.
2017. MARS GLOBAL CAVE CANDIDATE CATALOG (MGC^3). In *Astrobiology Science Conference*, Astrobiology Science Conference, P. 3708.

Cushing, G. E., C. H. Okubo, and T. N. Titus
2015. Atypical pit craters on Mars: New insights from THEMIS, CTX, and HiRISE observations. *Journal of Geophysical Research: Planets*, 120(6):1023–1043.

Ehlmann, B. L., J. F. Mustard, S. L. Murchie, J.-P. Bibring, A. Meunier, A. A. Fraeman, and Y. Langevin
2011. Subsurface water and clay mineral formation during the early history of Mars. *Nature*, 479:53–60.

Griffiths, R. W.
2000. The dynamics of lava flows. *Annual Review of Fluid Mechanics*, 32(1):477–518.

Hartmann, W. K. and G. Neukum
2001. Cratering Chronology and the Evolution of Mars. In *Chronology and Evolution of Mars*, R. Kallenbach, J. Geiss, and W. K. Hartmann, eds., Pp. 165–194, Dordrecht. Springer Netherlands.

Haruyama, J., K. Hioki, M. Shirao, T. Morota, H. Hiesinger, C. H. v. d. Bogert, H. Miyamoto, A. Iwasaki, Y. Yokota, M. Ohtake, T. Matsunaga, S. Hara, S. Nakanotani, and C. M. Pieters
2009. Possible lunar lava tube skylight observed by SELENE cameras. *Geophysical Research Letters*, 36(21).

Head, J. W., R. Greeley, M. P. Golombek, W. Hartmann, E. Hauber, R. Jaumann, P. L. Masson, G. Neukum, L. E. Nyquist, and M. H. Carr
2001. Geological Processes and Evolution. *Space Science Reviews*, 96:263–292.

Hiesinger, H., N. Bartel, T. Boas, D. Reiss, J. H. Pasckert, and C. H. van der Bogert
2015. Rheology and Ages of Lava Flows on Arsia and Pavonis Mons, Mars. In *EGU General Assembly Conference Abstracts*, EGU General Assembly Conference Abstracts, P. 9830.

Honda, T.
2018. Yield strength and lava tube cave height estimated from pits and lava flows of the Moon and Mars. In *PPS05-P13, JPGU-AGU Joint Meeting*.

Hulme, G.
1974. The interpretation of lava flow morphology. *Geophysical Journal of the Royal Astronomical Society*, 39(2):361–383.

Hulme, G.
1982. A review of lava flow processes related to the formation of lunar sinuous rilles. *Geophysical surveys*, 5(3):245–279.

Ivanov, B. A.
2001. Mars/Moon Cratering Rate Ratio Estimates. *Space Science Reviews*, 96(1):87–104.

Kaku, T., J. Haruyama, W. Miyake, A. Kumamoto, K. Ishiyama, T. Nishibori, K. Yamamoto, S. T. Crites, T. Michikami, Y. Yokota, et al.
2017. Detection of intact lava tubes at Marius Hills on the Moon by SELENE (Kaguya) Lunar Radar Sounder. *Geophysical Research Letters*, 44(20):10–155.

Kalita, H., S. Morad, A. Ravindran, and J. Thangavelautham
2018. Path planning and navigation inside off-world lava tubes and caves. In *2018 IEEE/ION Position, Location and Navigation Symposium (PLANS)*, Pp. 1311–1318.

Kempe, S.
2012. Volcanic rock caves. In *Encyclopedia of Caves*, Pp. 865 – 873.

Kempe, S., I. Bauer, P. Bosted, D. Coons, and R. Elhard
2010. Inflationary versus crusted-over roofs of pyroducts (lava tunnels). In *Proceedings 14th International Symposium on Vulcanospeleology*.

Kesner, S. B., J. Plante, P. J. Boston, T. Fabian, and S. Dubowsky
2007. Mobility and power feasibility of a microbot team system for extraterrestrial cave exploration. In *Proceedings 2007 IEEE International Conference on Robotics and Automation*, Pp. 4893–4898.

Léveillé, R. J. and S. Datta
2010. Lava tubes and basaltic caves as astrobiological targets on Earth and Mars: a review. *Planetary and Space Science*, 58(4):592–598.

Malin, M. C., J. F. Bell, B. A. Cantor, M. A. Caplinger, W. M. Calvin, R. T. Clancy, K. S. Edgett, L. Edwards, R. M. Haberle, P. B. James, S. W. Lee, M. A. Ravine, P. C. Thomas, and M. J. Wolff
2007. Context Camera Investigation on board the Mars Reconnaissance Orbiter. *Journal of Geophysical Research: Planets (1991–2012)*, 112(E5).

McEwen, A. S.
2018. THE FUTURE OF MRO/HIRISE. In *Lunar and Planetary Science Conference*, Lunar and Planetary Science Conference, P. 1301.

McEwen, A. S., E. M. Eliason, J. W. Bergstrom, N. T. Bridges, C. J. Hansen, W. A. Delamere, J. A. Grant, V. C. Gulick, K. E. Herkenhoff, L. Keszthelyi, R. L. Kirk, M. T. Mellon, S. W. Squyres, N. Thomas, and C. M. Weitz
2007. Mars Reconnaissance Orbiter's High Resolution Imaging Science Experiment (HiRISE). *Journal of Geophysical Research: Planets*, 112(E5).

McSween, H. Y., R. E. Arvidson, J. F. Bell, D. Blaney, N. A. Cabrol, P. R. Christensen, B. C. Clark, J. A. Crisp, L. S. Crumpler, D. J. Des Marais, J. D. Farmer, R. Gellert, A. Ghosh, S. Gorevan, T. Graff, J. Grant, L. A. Haskin, K. E. Herkenhoff, J. R. Johnson, B. L. Jolliff, G. Klingelhoefer, A. T. Knudson, S. McLennan, K. A. Milam, J. E. Moersch, R. V. Morris, R. Rieder, S. W. Ruff, P. A. de Souza, S. W. Squyres, H. Wänke, A. Wang, M. B. Wyatt, A. Yen, and J. Zipfel
2004. Basaltic Rocks Analyzed by the Spirit Rover in Gusev Crater. *Science*, 305(5685):842–845.

Melosh, H. J.
2011. *Planetary Surface Processes*, Cambridge Planetary Science. Cambridge University Press.

Moore, H. J., D. W. G. Arthur, and G. G. Schaber
1978. Yield strengths of flows on the Earth, Mars, and Moon. *Lunar and Planetary Science Conference Proceedings*, 3:3351–3378.

Neukum, G., B. Ivanov, and W. Hartmann
2001. Cratering Records in the Inner Solar System in Relation to the Lunar Reference System. *Space Science Reviews*, 96(1):55–86.

Neukum, G., R. Jaumann, H. Hoffmann, E. Hauber, J. Head, A. Basilevsky, B. Ivanov, S. Werner, S. Gasselt, J. Murray, and T. Mccord
2005. Recent and episodic volcanic and glacial activity on Mars revealed by the High Resolution Stereo Camera. *Nature*, 432:971–9.

Neumann, G. A., D. D. Rowlands, F. G. Lemoine, D. E. Smith, and M. T. Zuber
2001. Crossover analysis of Mars Orbiter Laser Altimeter data. *Journal of Geophysical Research: Planets*, 106(E10):23753–23768.

Neumann, G. A., M. T. Zuber, M. A. Wieczorek, P. J. McGovern, F. G. Lemoine, and D. E. Smith
2004. Crustal structure of Mars from gravity and topography. *Journal of Geophysical Research: Planets*, 109(E8).

Oberbeck, V. R., W. L. Quaide, and R. Greeley
1969. On the Origin of Lunar Sinuous Rilles. *Modern Geology*, 1:75–80.

Perry, M. R., N. E. Putzig, Z. M. Bain, D. A. Crown, S. P. Scheidt, and D. E. Nunes
2019. Detection and Characterization of Intact Lava Tubes on the Western Flank of Alba Mons in Mars Reconnaissance Orbiter Shallow Radar (SHARAD) Data. *LPI Contributions*, 2089:6405.

Plescia, J. B.
2004. Morphometric properties of Martian volcanoes. *Journal of Geophysical Research (Planets)*, 109(E3):E03003.

Pozzobon, R., F. Mazzarini, M. Massironi, and L. Marinangeli
2015. Self-similar clustering distribution of structural features on Ascraeus Mons (Mars): implications for magma chamber depth. *Geological Society, London, Special Publications*, 401(1):203–218.

Re, C., R. Roncella, G. Forlani, G. Cremonese, and G. Naletto
2012. Evaluation of area-based image matching applied to DTM generation with Hirise images. *Int. Arch. of Photogrammetry, Remote Sensing and Spatial Information Sciences*, 39:7.

Robbins, S. J., R. H. Hoover, and M. R. Kirchoff
2019. Fully Controlled 6 Meters/Pixel Mosaic of Mars' South Pole and Equator from Mars Reconnaissance Orbiter Context Camera, II. In *2019 Annual Meeting of Planetary Geologic Mappers*, volume 2154, P. 7022.

Robinson, M., J. Ashley, A. Boyd, R. Wagner, E. Speyerer, B. R. Hawke, H. Hiesinger, and C. van der Bogert
2012. Confirmation of sublunarean voids and thin layering in mare deposits. *Planetary and Space Science*, 69(1):18 – 27.

Rossi, A. P. and S. Van Gasselt
2018. *Planetary geology*. Springer.

Sauro, F., R. Pozzobon, P. Deberardinis, M. Massironi, and J. De Waele
2018. Morphometry of Terrestrial, Lunar, and Martian Lava Tube Candidates. In *Lunar and Planetary Science Conference*, Lunar and Planetary Science Conference, P. 1105.

Sauro, F., R. Pozzobon, T. Santagata, I. Tomasi, M. Tonello, J. Martínez-Frías, L. M. J. Smets, G. D. Santana Gómez, and M. Massironi
2019. *Volcanic Caves of Lanzarote: A Natural Laboratory for Understanding Volcano-Speleogenetic Processes and Planetary Caves*, Pp. 125–142. Cham: Springer International Publishing.

Seu, R., D. Biccari, R. Orosei, L. Lorenzoni, R. Phillips, L. Marinangeli, G. Picardi, A. Masdea, and E. Zampolini
2004. SHARAD: The MRO 2005 shallow radar. *Planetary and Space Science*, 52(1):157 – 166. Exploring Mars Surface and its Earth Analogues.

Shaw, H. R.
1969. Rheology of Basalt in the Melting Range1. *Journal of Petrology*, 10(3):510–535.

Simioni, E., C. Re, T. Mudric, A. Pommerol, N. Thomas, and G. Cremonese
2017. A PHOTOGRAMMETRIC PIPELINE FOR THE 3D RECONSTRUCTION OF CASSIS IMAGES ON BOARD EXOMARS TGO. *ISPRS - International Archives of the Photogrammetry, Remote Sensing and Spatial Information Sciences*, XLII-3/W1:133–139.

Simioni, E., C. Re, T. Mudrich, M. Pajola, A. Lucchetti, R. Pozzobon, P. Cambianica, G. Cremonese, A. Pommerol, and N. Thomas
2018. 3DPD application to the first CaSSIS DTMs.

Tanaka, K., J. J. Skinner, J. Dohm, R. Irwin, E. Kolb, C. Fortezzo, T. Platz, G. Michael, and T. Hare
2014. Geologic map of Mars. U.S. Geological Survey Scientific Investigations Map.

Thomas, N., G. Cremonese, R. Ziethe, M. Gerber, M. Brändli, G. Bruno, M. Erismann, L. Gambicorti, T. Gerber, K. Ghose, M. Gruber, P. Gubler, H. Mischler, J. Jost, D. Piazza, A. Pommerol, M. Rieder, V. Roloff, A. Servonet, W. Trottmann, T. Uthaicharoenpong, C. Zimmermann, D. Vernani, M. Johnson, E. Pelò, T. Weigel, J. Viertl, N. De Roux, P. Lochmatter, G. Sutter, A. Casciello, T. Hausner, I. Ficai Veltroni, V. Da Deppo, P. Orleanski, W. Nowosielski, T. Zawistowski, S. Szalai, B. Sodor, S. Tulyakov, G. Troznai, M. Banaskiewicz, J. C. Bridges, S. Byrne, S. Debei, M. R. El-Maarry, E. Hauber, C. J. Hansen, A. Ivanov, L. Keszthelyi, R. Kirk, R. Kuzmin, N. Mangold, L. Marinangeli, W. J. Markiewicz, M. Massironi, A. S. McEwen, C. Okubo, L. L. Tornabene, P. Wajer, and J. J. Wray
2017. The Colour and Stereo Surface Imaging System (CaSSIS) for the ExoMars Trace Gas Orbiter. *Space Science Reviews*, 212(3):1897–1944.

Werner, S. C.
2009. The global martian volcanic evolutionary history. *Icarus*, 201(1):44 – 68.

White, F.
2011. *Fluid Mechanics*, McGraw-Hill series in mechanical engineering. McGraw Hill.

Williams, K., C. McKay, O. Toon, and J. Head
2010. Do ice caves exist on Mars? *Icarus*, 209:358–368.

Wilson, L. and J. W. Head III
1994. Mars: Review and analysis of volcanic eruption theory and relationships to observed landforms. *Reviews of Geophysics*, 32(3):221–263.

Wilson, L. and J. W. Head III
2002. Tharsis-radial graben systems as the surface manifestation of plume-related dike intrusion complexes: Models and implications. *Journal of Geophysical Research: Planets*, 107(E8):1–1–1–24.

Wyatt, M. B. and H. Y. McSween
2002. Spectral evidence for weathered basalt as an alternative to andesite in the northern lowlands of Mars. *Nature*, 417:263–266.